Supporting Information

Achieving white light emission and increased magnetic anisotropy by transition metal substitution in functional materials based on dinuclear Dy^{III}(4-pyridone)$[M^{III}(CN)_6]^{3-}$ (M = Co, Rh) molecules

Junhao Wang,[a] Szymon Chorazy,*[,b] Koji Nakabayashi,[a] Barbara Sieklucka[b] and Shin-ich Ohkoshi,*[,a]

[a] *Department of Chemistry, School of Science, The University of Tokyo, 7-3-1 Hongo, Bunkyo-ku, Tokyo 113-0033, Japan.*

[b] *Faculty of Chemistry, Jagiellonian University, Gronostajowa 2, 30-387 Kraków, Poland.*

*Corresponding authors: ohkoshi@chem.s.u-tokyo.ac.jp; simon.chorazy@uj.edu.pl

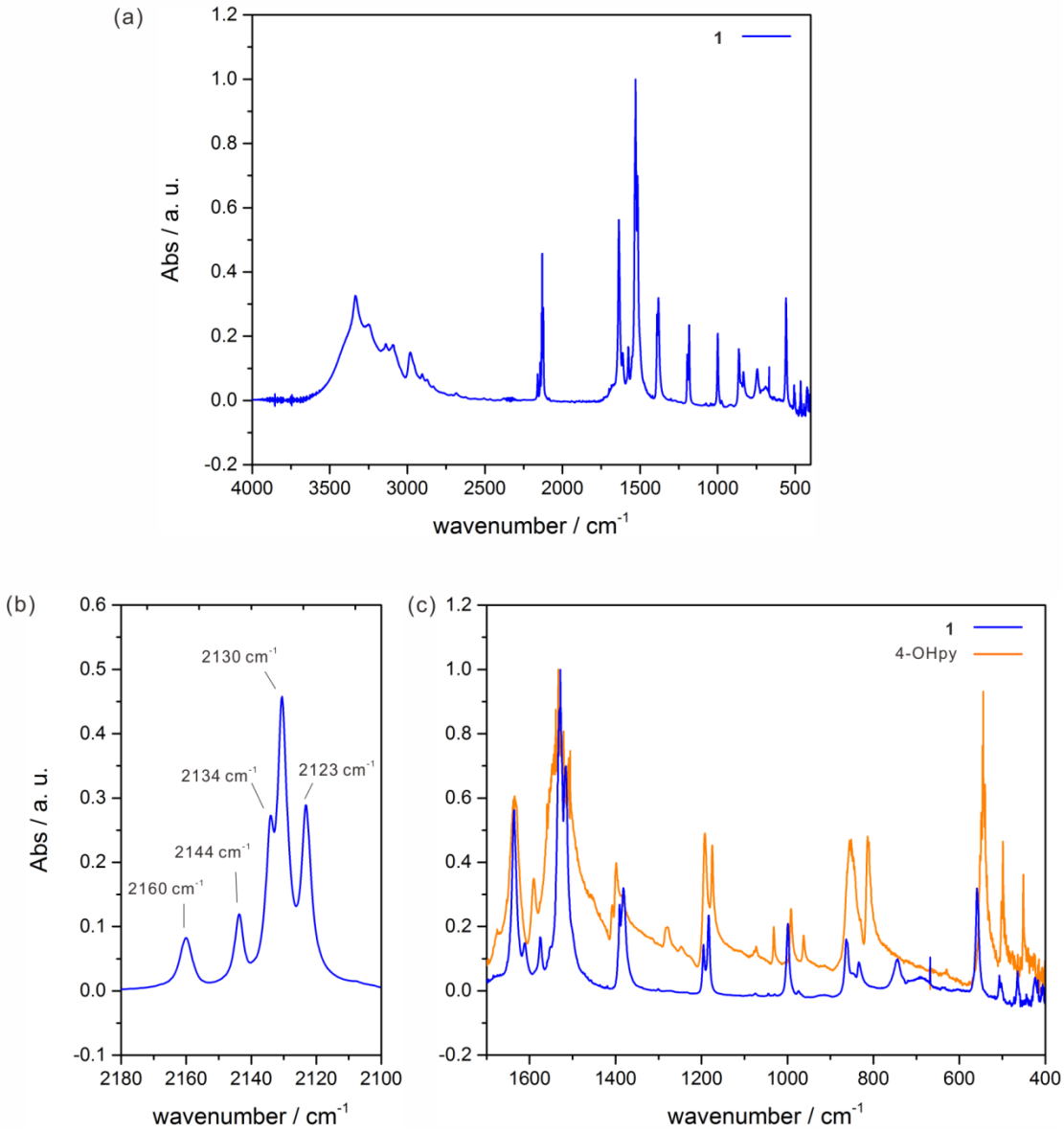

Figure S1 Infrared absorption spectrum of **1** (blue line): (*a*) the whole wavenumber measurement scope of 4000-400 cm^{-1}, (*b*) the 2180-2100 cm^{-1} part of the spectrum showing the stretching vibrations of cyanides, and (*c*) the 1700-400 cm^{-1} part of the spectrum showing the vibrations of the 4-pyridone organic ligand. The characteristic absorption peaks for free 4-hydroxypyridine was presented for the comparison in (*c*) (orange line).

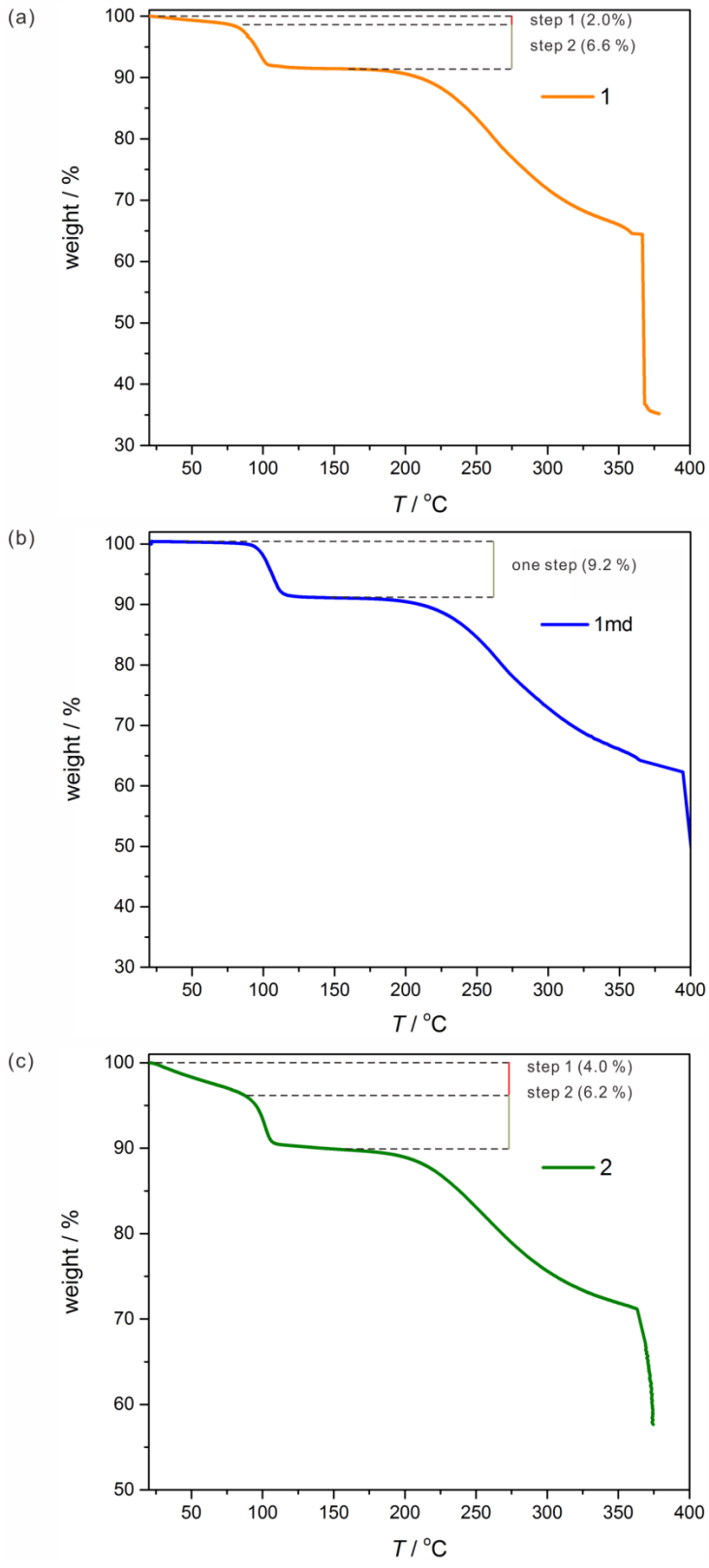

Figure S2 Thermogravimetric curves measured under an air atmosphere in the temperature range of 20-400 °C of **1** (*a*), magnetically diluted **1md** (*b*, see description below Figure S13 for details), and **2** (*c*), with the indicated steps related to the loss of water molecules on heating process (see the comment on the next page).

Comment to Figure S2

Figure S2 (*a*): on the heating process from 20 °C to 83 °C (step 1) the graduate decrease of mass of **1** from 100 % to 98.0 % (weight loss of 2.0 %, step 1) corresponds to the removal of weakly weakly-bonded, non-coordinated water molecules in the amount of one molecule per one $\{Dy^{III}Co^{III}\}$ unit (calcd. 2.2 %). Further heating leads to the abrupt decrease in the narrow temperature range of 85-105 °C from 98.0 % to 91.4 % (weight loss of 6.6 %, step 2) which is ascribed to the removal of hydrogen bonded water molecules in the amount of one, and two coordinated water molecules per one $\{Dy^{III}Co^{III}\}$ unit (calcd. 6.5 %). Therefore, the two found steps of weight loss in TGA curve is in good agreement with the composition of **1**, $[Dy^{III}(4\text{-pyridone})_4(H_2O)_2][Co^{III}(CN)_6]\cdot 2H_2O$, determined by the CHN elemental analysis. The subsequent plateau in the TGA curve indicates the further stability of the dehydrated phase in the presumable formula of $\{[Dy^{III}(4\text{-pyridone})_4][Co^{III}(CN)_6]\}$ up to 185 °C.

Figure S2 (*b*): on the heating process from 20 °C to 90 °C, **1md** was survived without any decrease of mass. Further heating leads to the abrupt decrease in the narrow temperature range of 90-116 °C from 100 % to 90.8 % (weight loss of 9.2 %, one) which correspond to the simultaneous removal of two crystallization, and two coordinated water molecules per one $\{Dy^{III}_{0.12}Y^{III}_{0.88}Co^{III}\}$ unit (calcd. 9.4 %). Therefore, the found one step of weight loss in TGA curve is in good agreement with the composition of **1md**, $[(Dy^{III}_{0.12}Y^{III}_{0.88})(4\text{-pyridone})_4(H_2O)_2][Co^{III}(CN)_6]\cdot 2H_2O$, determined by the CHN elemental analysis. The subsequent plateau in the TGA curve indicates the thermal stability of the dehydrated phase in the presumable formula of $\{[Dy_{0.12}{}^{III}Y^{III}_{0.88}(4\text{-pyridone})_4][Co^{III}_{0.88}(CN)_6]\}$ up to 190 °C.

Figure S2 (*c*): on the heating process from 20 °C to 89 °C (step 1) the graduate decrease of mass of **2** from 100 % to 96.0 % (weight loss of 4.0 %, step 1) corresponds to the removal of three weakly-bonded, non-coordinated water molecules per one $\{Dy^{III}Rh^{III}\}$ unit (calcd. 4.0 %). Further heating leads to the abrupt decrease in the narrow temperature range of 89-110 °C from 96.0 % to 89.8 % (weight loss of 6.2 %, step 2) which is ascribed to the removal of one crystallization water molecules, and two coordinated water molecules per one $\{Dy^{III}Rh^{III}\}$ unit (calcd. 6.2 %). Therefore, the two found steps of weight loss in TGA curve agree well with the composition of **2**, $\{[Dy^{III}(4\text{-pyridone})_4\cdot(H_2O)_2]\ [Rh^{III}(CN)_6]\}\cdot 4H_2O$, determined by the CHN elemental analysis. The subsequent plateau in the TGA curve indicates the survival of the dehydrated phase in the presumable formula of $\{[Dy^{III}(4\text{-pyridone})_4]\ [Rh^{III}(CN)_6]\}$ up to 194 °C.

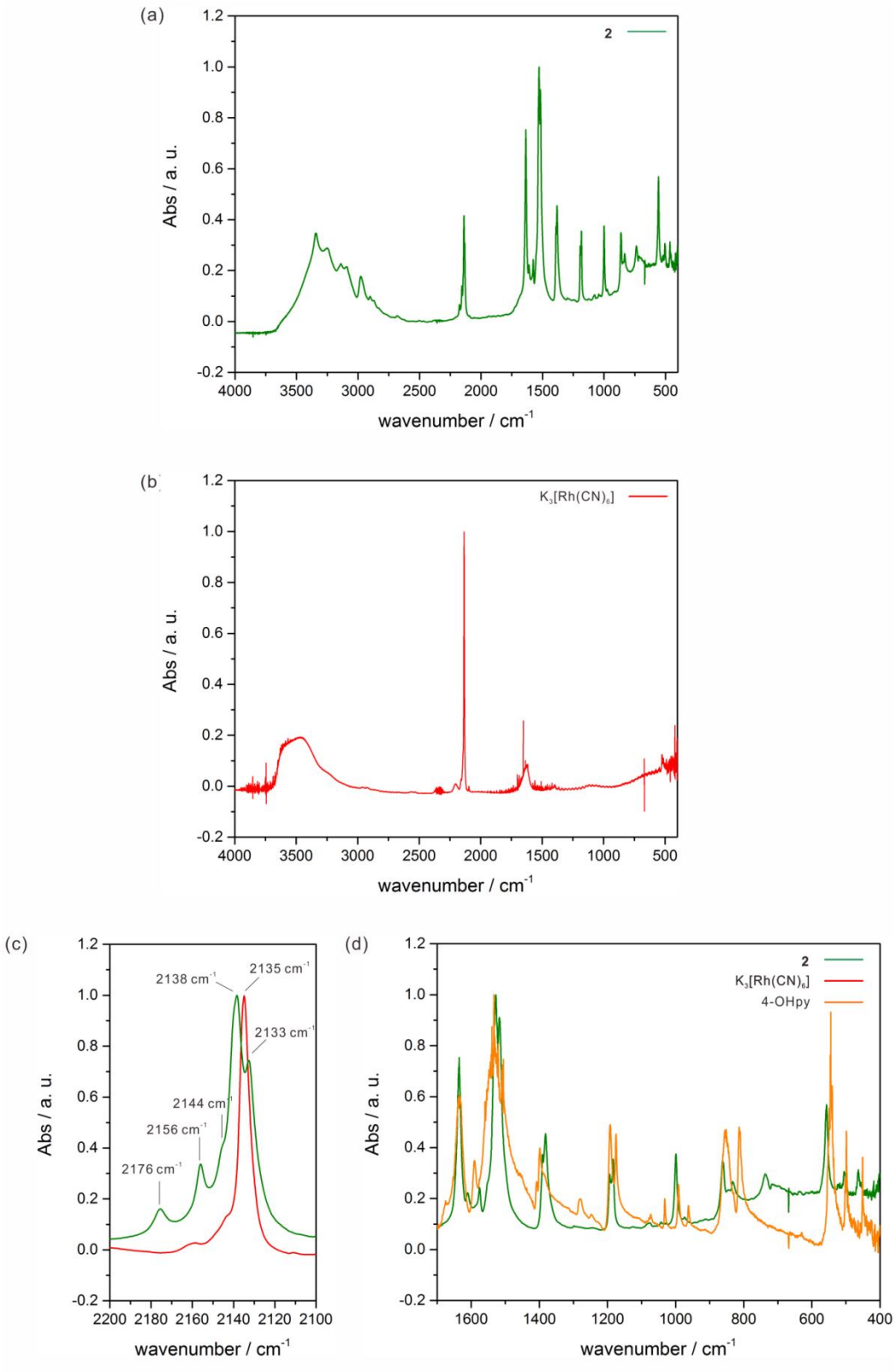

Figure S3 Infrared absorption spectrum of **2** (green line) in the 4000-400 cm^{-1} range (*a*) confronted with the related spectrum for the starting material, $K_3[Rh^{III}(CN)_6]$ (red line) (*b*), and the detailed comparison views: (*c*) between **2** and $K_3[Rh^{III}(CN)_6]$ in the limited 2200-2100 cm^{-1} range of the stretching vibrations of cyanides, and (*d*) between **2** and free 4-hydroxypyridine in the limited 1700-400 cm^{-1} range.

Table S1 Crystal data and structure refinement of **1** and **2**.

compound		**1**	**2**
method		single-crystal XRD	single-crystal XRD
formula		$Dy_1Co_1C_{26}H_{28}O_8N_{10}$	$Dy_1Rh_1C_{26}H_{28}O_8N_{10}$
formula weight [g·mol^{-1}]		830.01	873.99
T [K]		90(2)	90(2)
λ [Å]		0.71075 (Mo Kα)	0.71075 (Mo Kα)
crystal system		orthorhombic	orthorhombic
space group		Cmc2_1 (No. 36)	Cmc2_1 (No. 36)
unit cell	$\boldsymbol{a}$ [Å]	14.8064(6)	14.8508(9)
	$\boldsymbol{b}$ [Å]	14.9660(4)	15.1527(10)
	$\boldsymbol{c}$ [Å]	14.0417(4)	14.0756(10)
	$\boldsymbol{\alpha}$ [deg]	90	90
	$\boldsymbol{\beta}$ [deg]	90	90
	$\boldsymbol{\gamma}$ [deg]	90	90
flack parameter		0.493(8)	0.45(2)
V [Å^3]		3111.54(18)	3167.4(4)
Z		4	4
calculated density [g·cm^{-3}]		1.772	1.833
absorption coefficient [mm^{-1}]		2.980	2.925
F(100)		1644.0	1716.0
crystal size [mm × mm × mm]		0.364 × 0.376 × 0.119	0.058 × 0.067 × 0.201
θ range [deg]		(3.085, 27.471)	(3.054, 27.478)
limiting indices		-19 < h < 19 -19 < k < 17 -19 < l < 18	-19 < h < 17 -19 < k < 19 -18 < l < 18
collected reflections		14956	24918
unique reflections		3699	3759
R_{int}		0.0126	0.0831
completeness		1.91/1.00	1.92/1.00
max. and min. transmission		0.755 and 0.923	0.755 and 0.879
refinement method		full-matrix least squares on F^2	full-matrix least squares on F^2
data/restraints/parameters		3699/98/324	3759/122/323
GOF on F^2		0.895	1.101
final R indices		R_1 = 0.0145 [I > 2σ(I)] wR_2 = 0.0288 (all data)	R_1 = 0.0456 [I > 2σ(I)] wR_2 = 0.0689 (all data)
largest diff peak and hole		0.479 and -0.758 e·A^{-3}	1.136 and -2.379 e·A^{-3}

Table S2 Detailed structural parameters of **1**.

$[Dy^{III}(4\text{-pyridone})_4(\mu\text{-NC})(H_2O)_2]^{2+}$ complex		$[Co^{III}(CN)_6]^{3-}$ complex	
parameter	value [Å, ˚]	parameter	value [Å, ˚]
Dy1-O1	2.402(2)	Co1-C1	1.891(3)
Dy1-O2	2.298(17)	Co1-C2	1.902(4)
Dy1-O3	2.266(18)	Co1-C3	1.903(16)
Dy1-O4	2.242(14)	Co1-C4	1.899(15)
Dy1-O5	2.232(15)	Co1-C5a	1.815(17)
Dy1-N1	2.483(3)	Co1-C5b	1.980(12)
C1-N1-Dy1	175.9(17)	C1-N1	1.1528
O4-Dy1-O1	75.0(4)	C2-N2	1.1443
O4-Dy1-O1	97.1(6)	C3-N3	1.1011
O4-Dy1-O3	89.65	C4-N4	1.1973
O4-Dy1-N1	95.3(6)	C5a-N5a	1.3145
O4-Dy1-O2	93.9(6)	C5b-N5b	1.0377
O5-Dy1-N1	97.7(6)	N1-C1-Co1	176(2)
O5-Dy1-O2	88.87	C1-Co1-C3	91.3(8)
O5-Dy1-O1	93.4(6)	C1-Co1-C4	89.4(8)
O5-Dy1-O1	72.6(6)	C1-Co1-C5a	89.7(6)
O5-Dy1-O3	95.2(6)	C1-Co1-C5b	89.4(4)
N1-Dy1-O2	74.3(4)	C2-Co1-C3	89.3(8)
O2-Dy1-O1	72.2(4)	C2-Co1-C4	90.1(8)
O1-Dy1-O1	71.32(11)	C2-Co1-C5a	90.2(6)
O1-Dy1-O3	75.0(4)	C2-Co1-C5b	90.7(4)
O3-Dy1-N1	71.7(4)	Co1-C1-N1	176(2)
O2-Dy1-O1	137.6(5)	Co1-C2-N2	180(2)
O2-Dy1-O3	146	Co1-C3-N3	179.7(15)
O1-Dy1-O3	140.8(5)	Co1-C4-N4	179.1(14)
O1-Dy1-N1	144.33(6)	Co1-C5a-N5a	174.1(19)
O4-Dy1-O5	166.94	Co1-C5b-N5b	176.5(15)
N1-Dy1-O1	144.33(6)	Co1-Dy1 (C1-N1)	5.525

Table S3 Detailed structural parameters of **2**.

$[Dy^{III}(4\text{-pyridone})_4(\mu\text{-NC})(H_2O)_2]^{2+}$ complex		$[Rh^{III}(CN)_6]^{3-}$ complex	
parameter	value [Å, ˚]	parameter	value [Å, ˚]
Dy1-O1	2.393(6)	Rh1-C1	1.966(12)
Dy1-O2	2.35(3)	Rh1-C2	2.076(12)
Dy1-O3	2.24(3)	Rh1-C3	2.05(4)
Dy1-O4	2.26(3)	Rh1-C4	2.00(3)
Dy1-O5	2.21(3)	Rh1-C5a	2.09(4)
Dy1-N1	2.461(10)	Rh1-C5b	1.95(4)
C1-N1-Dy1	167.84	C1-N1	1.224
O4-Dy1-O1	79.9(7)	C2-N2	1.073
O4-Dy1-O1	100.2(7)	C3-N3	1.206
O4-Dy1-O3	89.47	C4-N4	1.064
O4-Dy1-N1	95.8(10)	C5a-N5a	1.057
O4-Dy1-O2	96.4(10)	C5b-N5b	1.256
O5-Dy1-N1	93.4(10)	N1-C1-Rh1	165(2)
O5-Dy1-O2	88.59	C1-Rh1-C3	96.5(12)
O5-Dy1-O1	94.2(7)	C1-Rh1-C4	84.3(12)
O5-Dy1-O1	70.6(8)	C1-Rh1-C5a	87.2(10)
O5-Dy1-O3	91.0(12)	C1-Rh1-C5b	92.2(11)
N1-Dy1-O2	75.0(8)	C2-Rh1-C3	90.2(14)
O2-Dy1-O1	70.3(7)	C2-Rh1-C4	89.0(14)
O1-Dy1-O1	70.5(3)	C2-Rh1-C5a	92.1(9)
O1-Dy1-O3	77.4(9)	C2-Rh1-C5b	88.6(11)
O3-Dy1-N1	71.1(9)	Rh1-C1-N1	165(2)
O2-Dy1-O1	133.6(8)	Rh1-C2-N2	180(4)
O2-Dy1-O3	146.02	Rh1-C3-N3	175(3)
O1-Dy1-O3	143.5(9)	Rh1-C4-N4	174(3)
O1-Dy1-N1	144.3(2)	Rh1-C5a-N5a	177(3)
O4-Dy1-O5	170.4	Rh1-C5b-N5b	171(4)
N1-Dy1-O1	144.3(2)	Dy1-Rh1	5.624

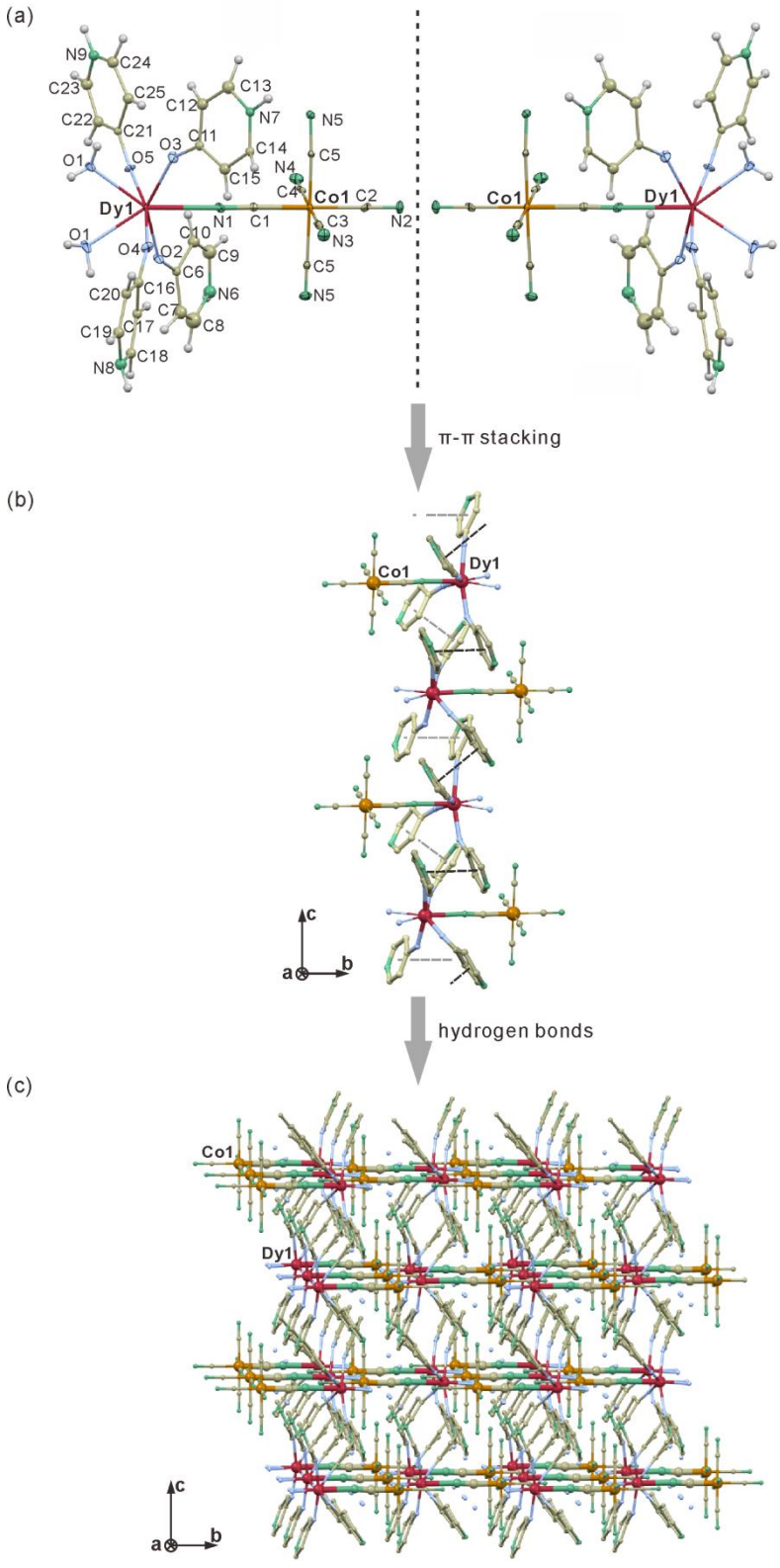

Figure S4 The structural views showing the formation of the three-dimensional supramolecular network of **1**: (a) the mirror-imaged enantiomers of dinuclear molecules coexisting in the crystal structure, (b) one-dimensional supramolecular chain along *c* direction stabilized by π-π interactions indicated by dashed lines, and (c) the three-dimensional supramolecular network presented within the *bc* crystallographic plane. The crystal structure of **2** is analogous to the presented above for **1**, with Rh^{III} replacing the Co^{III} metal center.

Table S4 Results of Continuous Shape Measure Analysis for $[Dy^{III}(4\text{-pyridone})_4(\mu\text{-NC})(H_2O)_2]^{2+}$ complexes in **1** and **2**.

Dy complex	CSM parameter				geometry
	PBPY-7	COC-7	CTPR-7	JPBPY-7	
1	1.382	6.044	4.513	4.306	PBPY-7
2	1.470	5.483	4.219	4.192	PBPY-7

*** CSM parameters:** [S1]

CSM PBPY-7 = the parameter related to the pentagonal bipyramid geometry (D_{5h} symmetry)

CSM COC-7: = the parameter related to the capped octahedron geometry (C_{3v} symmetry)

CSM CTPR-7: = the parameter related to the capped trigonal prism geometry (C_{2v} symmetry)

CSM JPBPY-7: = the parameter related to the Johnson pentagonal bipyramid geometry (J13, D_{5h} symmetry)

CSM = 0 for the ideal geometry; the increase of CSM parameter is related to the increasing distortion from the ideal polyhedron.

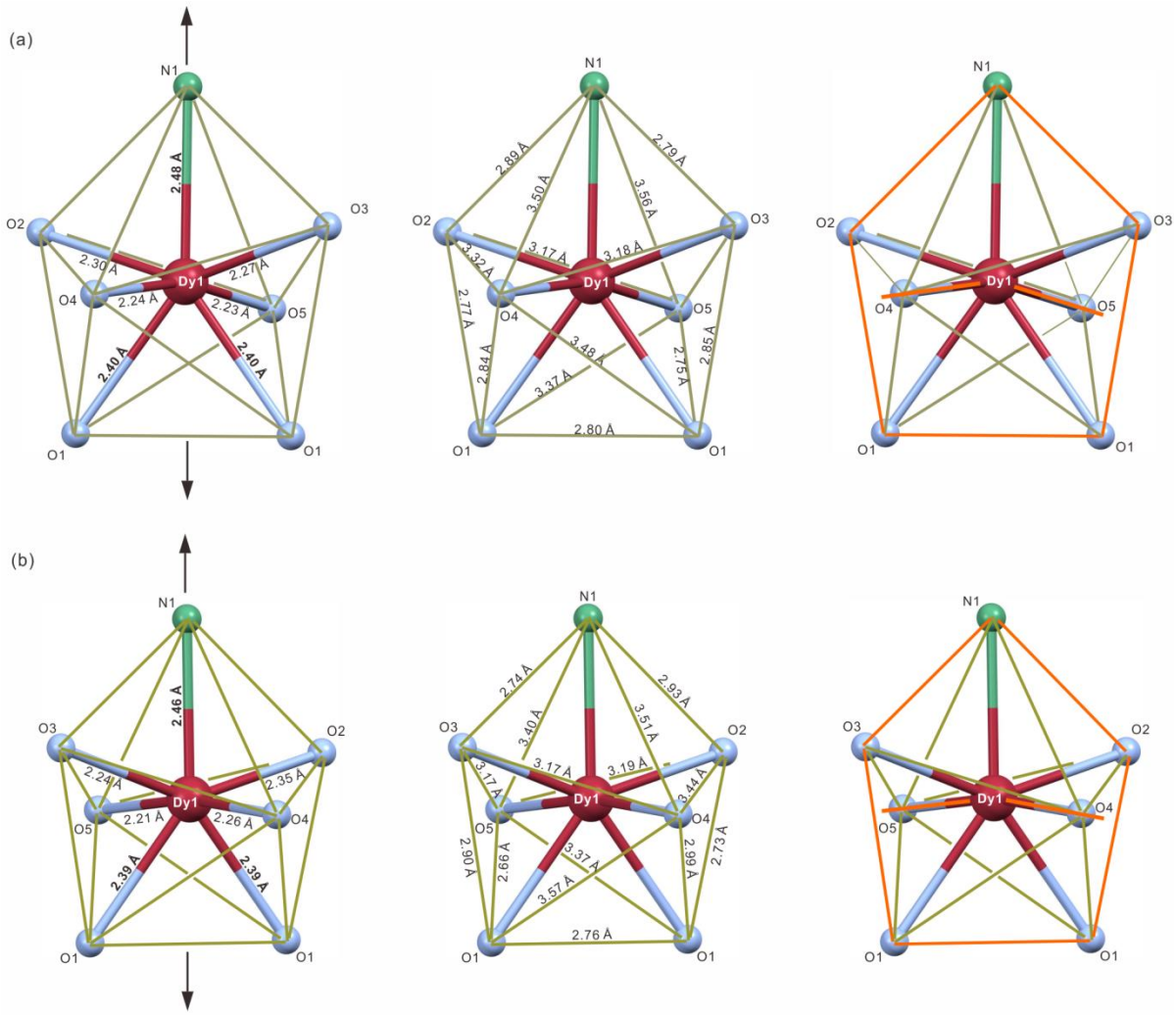

Figure S5 Detailed insight into the geometry of $[Dy^{III}(4\text{-pyridone})_4(\mu\text{-NC})(H_2O)_2]^{2+}$ complexes in **1** (*a*), and **2** (*b*): the arrangement of bond lengths within the coordination polyhedron with the indicated elongation directions (black arrows, left), the detailed dimensions of the polyhedron of the distorted PBPY-7 geometry (middle), and the visualization of the PBPY-8 coordination polyhedron (right).

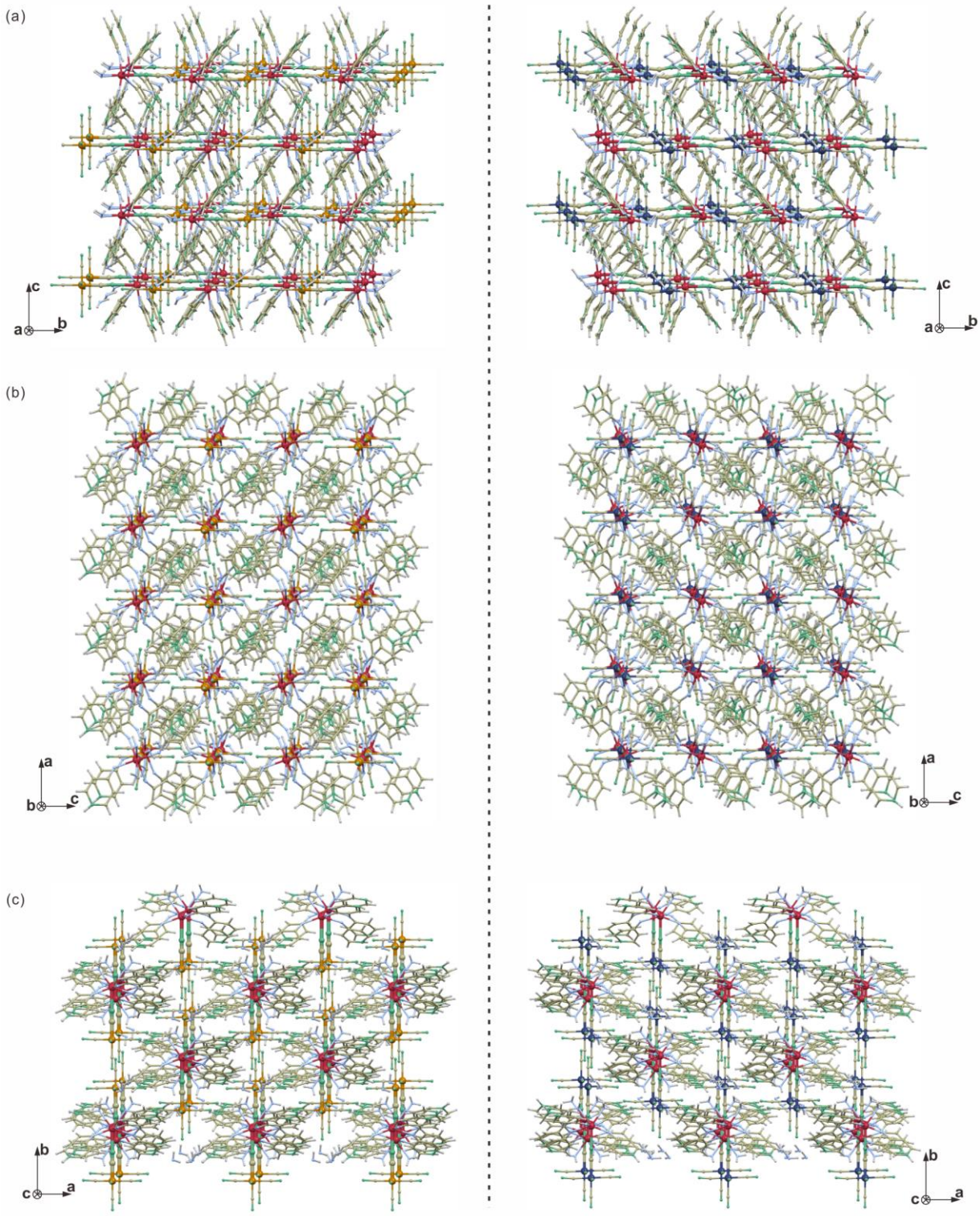

Figure S6 The spatial arrangement of dinuclear molecules of **1** (left) and **2** (right) in the supramolecular network presented along the directions of ***a*** axis (*a*), ***b*** axis (*b*), and ***c*** axis (*c*). The selected alignments of 4-pyridone ligands coordinated to Dy^{III} centers in **1** and **2** are the mirror images of each other. Colours: Dy, red; Co, brown; Rh, deep blue; C, dark yellow; N, green; O, light blue; H, light grey.

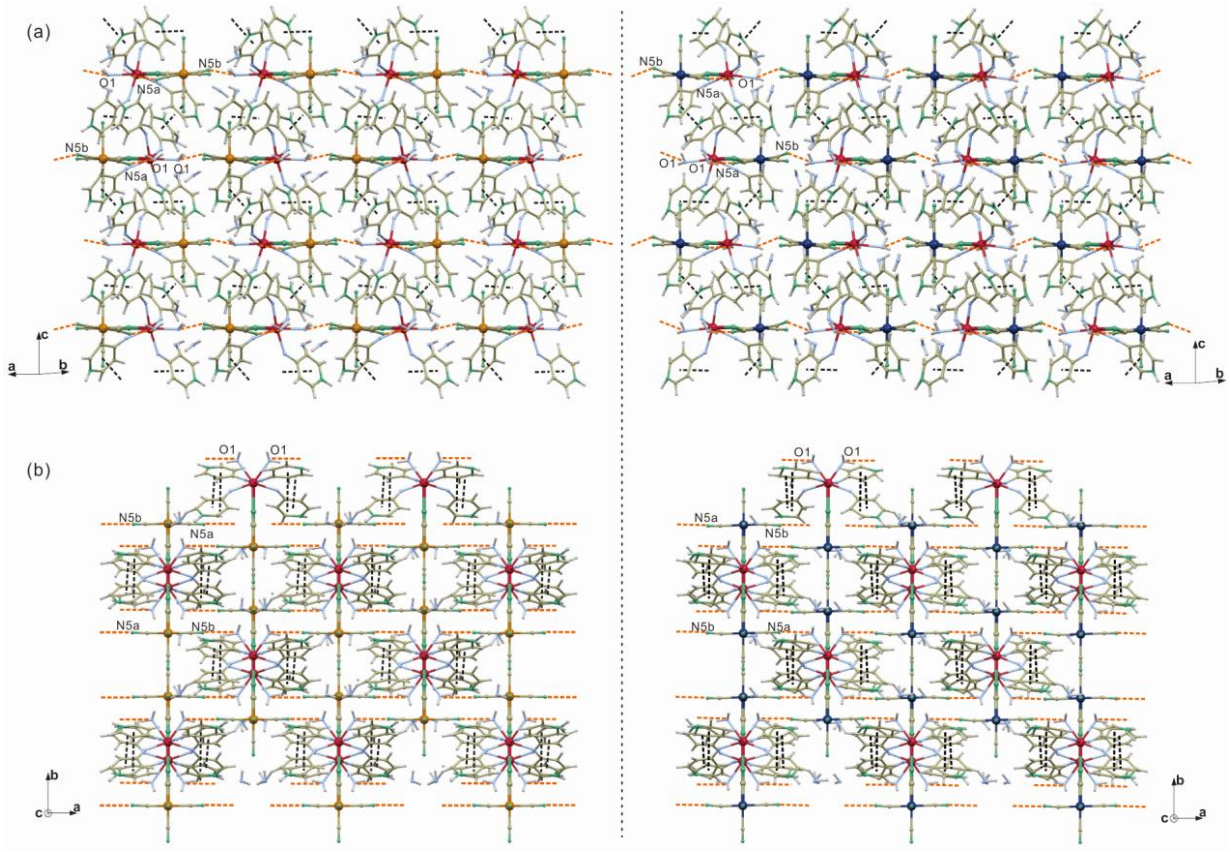

Figure S7 The noncovalent interactions between dinuclear molecules in the supramolecular networks of **1** (left) and **2** (right) including the hydrogen bonding between water molecules and cyanides (OH···NC, orange dashed lines), and π-π interactions between the 4-pyridone rings (black dashed lines), in the view within the (110) plane (*a*) and the (001) plane (*b*). Distances between centers involved in hydrogen bonds: **1**, O1-N5a, 2.94 Å; O1-N5b, 3.04 Å; **2**, O1-N5a, 2.92 Å; O1-N5b, 3.00 Å. Average distances between centers of 4-pyridone rings: **1**, 3.5 Å; **2**, 3.5 Å. Colours: Dy, red; Co, brown; Rh, deep blue; C, dark yellow; N, green; O, light blue; H, light grey.

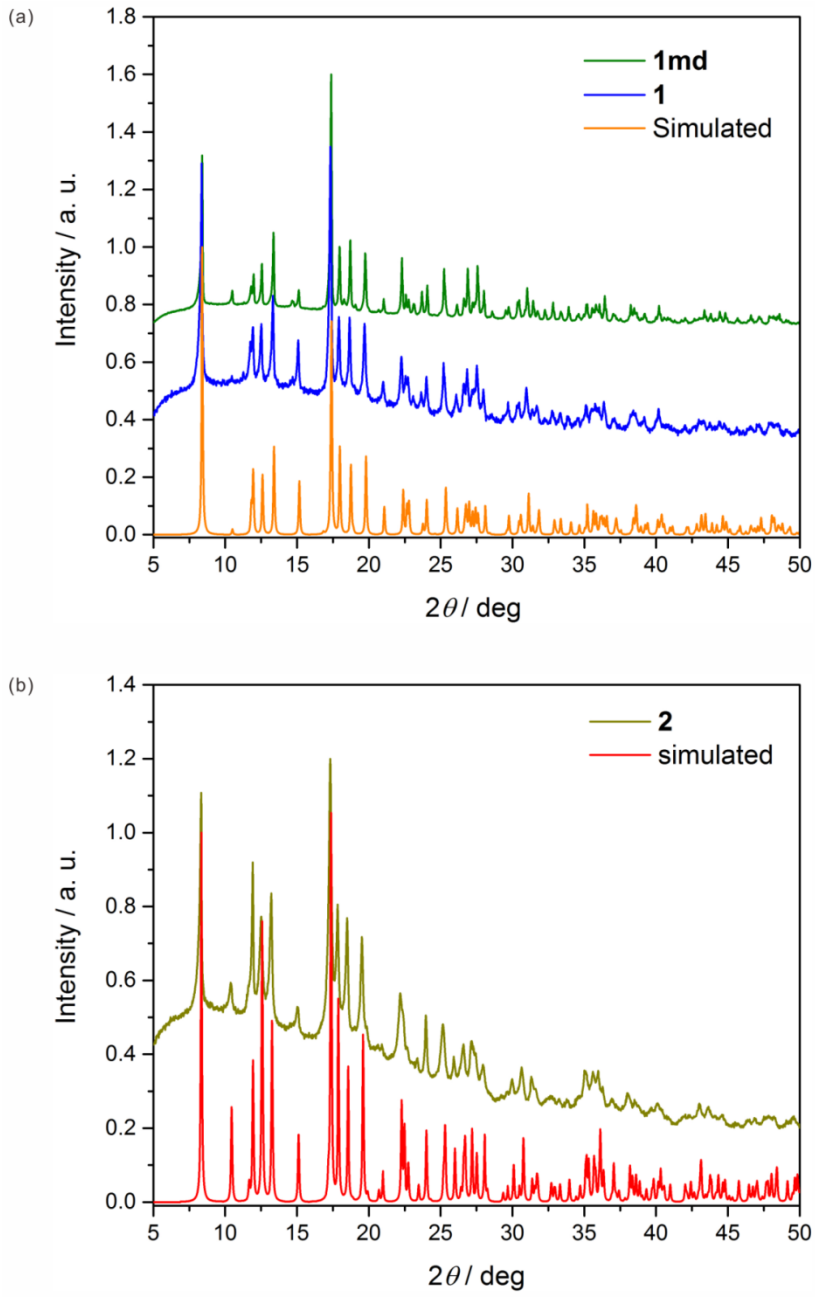

Figure S8 The experimental powder X-ray diffraction patterns of **1** (*a*, blue line), and its magnetically diluted sample, **1md** (*a*, green line) compared with the simulated pattern based on the single-crystal XRD structural model of **1** (*a*, orange line), and the experimental powder X-ray diffraction pattern of **2** (*b*, dark yellow line) compared with the simulated pattern based on the single-crystal XRD model of **2** (*b*, red line).

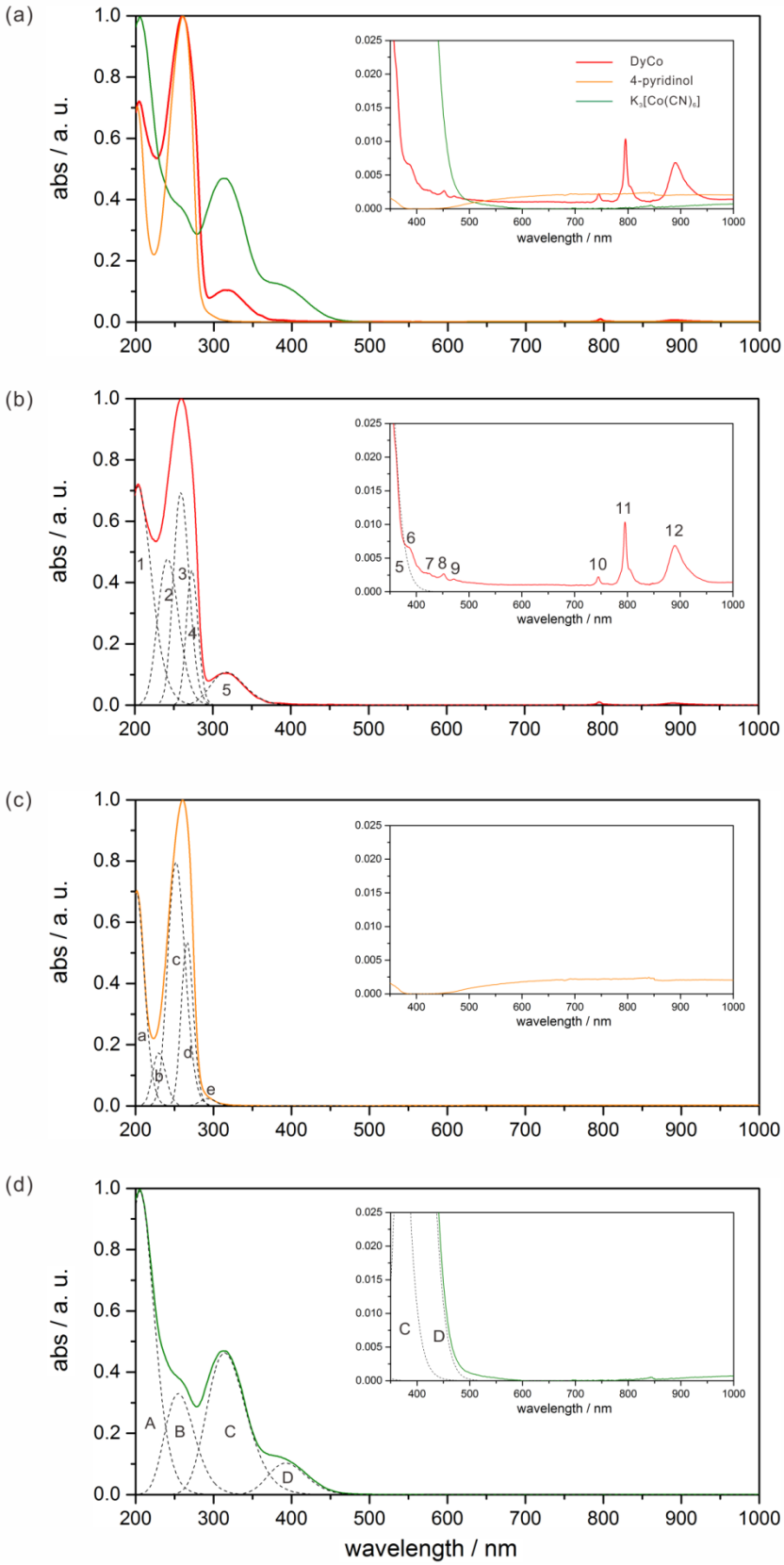

Figure S9 Solid state UV-vis-NIR absorption spectra of **1** (*a*-*b*, red line) compared with the spectra of 4-pyridone (*a*, *c*, orange line), and $K_3[Co^{III}(CN)_6]$ (*a*, *d*, green line). The experimental data were shown as the solid lines, while the deconvoluted components are illustrated as black dashed lines (see Table S5).

Table S5 Analysis of solid state UV-vis-NIR absorption spectrum of **1** compared with the analyses of the related spectra of the references, that are 4-pyridone and $K_3[Co^{III}(CN)_6]$ (see Figure S8).

compound	peak no.	λ_{max} [nm]	E_{max} [cm^{-1}]	interpretation
1	1	204	40920	combined contribution from M→L charge transfer of $[Co^{III}(CN)_6]$: $t_{2g} \rightarrow t_{1u}\pi^*$ and singlet to singlet transition of 4-pyridone: $\pi \rightarrow \pi^*$
	2	242	41320	combined contribution from d-d of $Co^{III\text{-}LS}$: $A_{1g} \rightarrow {}^1T_{2g}$ and singlet to singlet transition of 4-pyridone: $\pi \rightarrow \pi^*$
	3	259	38610	singlet to singlet transition of 4-pyridone: $\pi \rightarrow \pi^*$
	4	273	36630	combined contribution from d-d of $Co^{III\text{-}LS}$: $A_{1g} \rightarrow {}^1T_{1g}$ and singlet to singlet transition of 4-pyridone: $\pi \rightarrow \pi^*$
	5	317	31550	combined contribution from d-d of $Co^{III\text{-}LS}$: $A_{1g} \rightarrow {}^3T_{1g}$ and singlet to triplet transition of 4-pyridone: $\pi \rightarrow \pi^*$
	6	386	25910	f-f of Dy^{III}:[S2] ${}^6H_{15/2} \rightarrow {}^4I_{13/2}$
	7	425	23530	f-f of Dy^{III}: ${}^6H_{15/2} \rightarrow {}^4G_{11/2}$
	8	452	22120	f-f of Dy^{III}: ${}^6H_{15/2} \rightarrow {}^4I_{15/2}$
	9	471	21230	f-f of Dy^{III}: ${}^6H_{15/2} \rightarrow {}^4F_{9/2}$
	10	745	13420	f-f of Dy^{III}: ${}^6H_{15/2} \rightarrow {}^6F_{3/2}$
	11	795	12580	f-f of Dy^{III}: ${}^6H_{15/2} \rightarrow {}^6F_{5/2}$
	12	890	11240	f-f of Dy^{III}: ${}^6H_{15/2} \rightarrow {}^6F_{7/2}$
4-pyridone	a	201	49640	singlet to singlet transition:[S3] $\pi \rightarrow \pi^*$
	b	230	43500	
	c	252	39700	
	d	266	37570	
	e	292	34200	singlet to triplet transition: $\pi \rightarrow \pi^*$
$K_3[Co(CN)_6]$	A	205	48780	M→L charge transfer of $[Co^{III}(CN)_6]$:[S4] $t_{2g} \rightarrow t_{1u}\pi^*$
	B	255	39200	d-d of $Co^{III\text{-}LS}$: ${}^1A_{1g} \rightarrow {}^1T_{2g}$ (minor contribution of ${}^1A_{1g} \rightarrow {}^5T_{2g}$)
	C	314	31850	d-d of $Co^{III\text{-}LS}$: ${}^1A_{1g} \rightarrow {}^1T_{1g}$ (minor contribution of ${}^1A_{1g} \rightarrow {}^3T_{2g}$)
	D	393	25450	d-d of $Co^{III\text{-}LS}$: ${}^1A_{1g} \rightarrow {}^3T_{1g}$

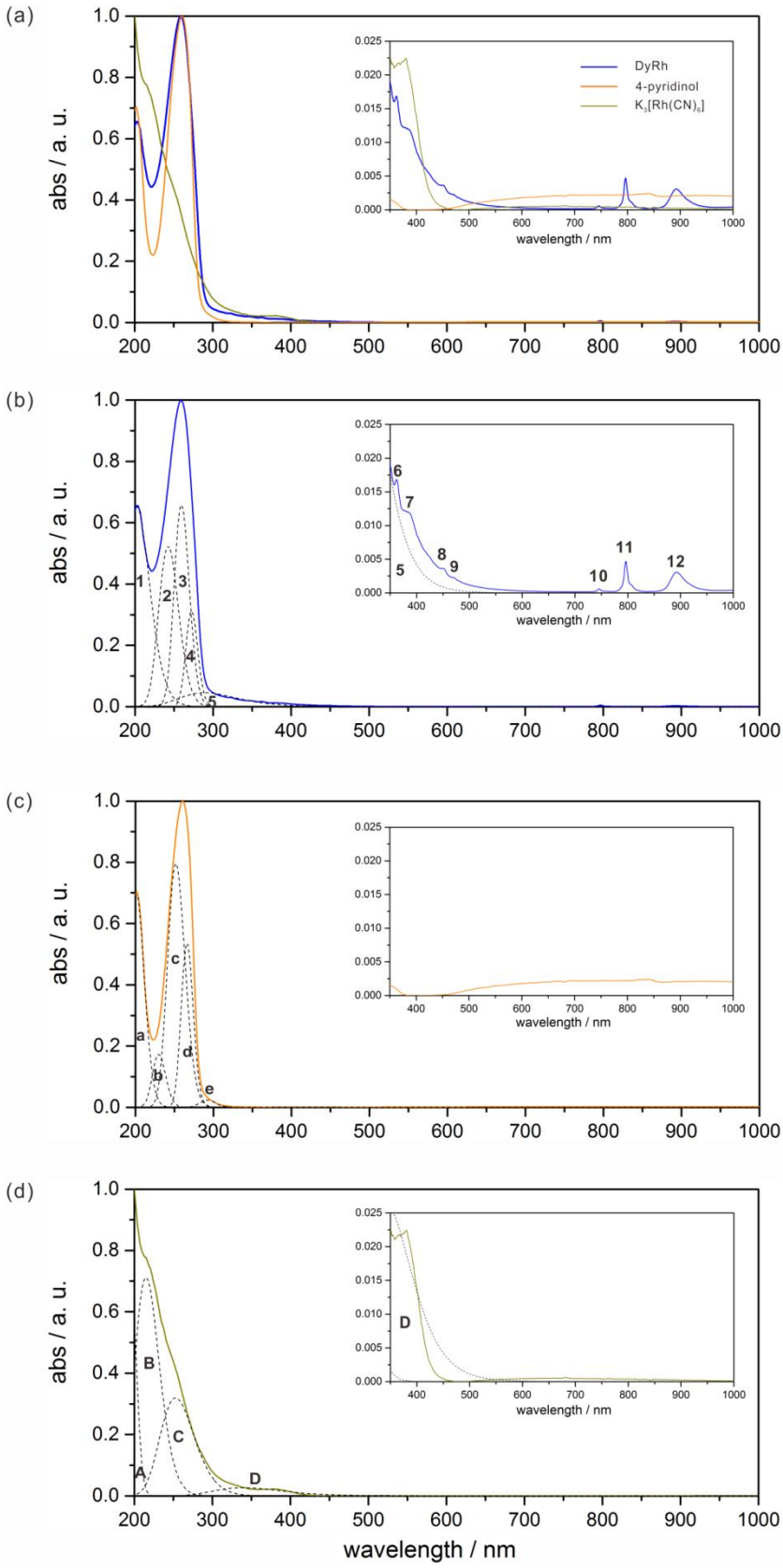

Figure S10 Solid state UV-vis-NIR absorption spectra of **2** (*a*-*b*, blue line) compared with the spectra of 4-pyridone (*a*, *c*, orange line), and $K_3[Rh^{III}(CN)_6]$ (*a*, *d*, dark yellow line). The experimental data were shown as the solid lines, while the deconvoluted components are illustrated as black dashed lines (see Table S6).

Table S6 Analysis of solid state UV-vis-NIR absorption spectrum of **2** compared with the analyses of the related spectra of the references, that are 4-pyridone and $K_3[Rh^{III}(CN)_6]$ (see Figure S9).

compound	peak no.	λ_{max} [nm]	E_{max} [cm^{-1}]	interpretation
2	1	202	49500	combined contribution from M→L charge transfer of $[Rh^{III}(CN)_6]$: $t_{2g} \rightarrow t_{1u}\pi^*$ and singlet to singlet transition of 4-pyridone: $\pi \rightarrow \pi^*$
	2	242	41320	combined contribution from d-d of $Rh^{III\text{-}LS}$: $A_{1g} \rightarrow {}^1T_{2g}$ and singlet to singlet transition of 4-pyridone: $\pi \rightarrow \pi^*$
	3	259	38610	singlet to singlet transition of 4-pyridone: $\pi \rightarrow \pi^*$
	4	272	36630	combined contribution from d-d of $Rh^{III\text{-}LS}$: $A_{1g} \rightarrow {}^1T_{1g}$ and singlet to singlet transition of 4-pyridone: $\pi \rightarrow \pi^*$
	5	289	34600	combined contribution from d-d of $Rh^{III\text{-}LS}$: $A_{1g} \rightarrow {}^3T_{1g}$ and singlet to triplet transition of 4-pyridone: $\pi \rightarrow \pi^*$
	6	362	27620	f-f of Dy^{III}.[S2] ${}^6H_{15/2} \rightarrow {}^4M_{19/2} + {}^4P_{5/2}$
	7	387	25840	f-f of Dy^{III}: ${}^6H_{15/2} \rightarrow {}^4I_{13/2}$
	8	452	22120	f-f of Dy^{III}: ${}^6H_{15/2} \rightarrow {}^4I_{15/2}$
	9	471	21230	f-f of Dy^{III}: ${}^6H_{15/2} \rightarrow {}^4F_{9/2}$
	10	745	13420	f-f of Dy^{III}: ${}^6H_{15/2} \rightarrow {}^6F_{3/2}$
	11	797	12550	f-f of Dy^{III}: ${}^6H_{15/2} \rightarrow {}^6F_{5/2}$
	12	892	11210	f-f of Dy^{III}: ${}^6H_{15/2} \rightarrow {}^6F_{7/2}$
4-pyridone	a	201	49640	singlet to singlet transition:[S3] $\pi \rightarrow \pi^*$
	b	230	43500	
	c	252	39700	
	d	266	37570	
	e	292	34200	singlet to triplet transition: $\pi \rightarrow \pi^*$
$K_3[Rh(CN)_6]$	A	197	50780	M→L charge transfer:[S4] $t_{2g} \rightarrow t_{1u}\pi^*$
	B	215	46500	d-d of $Rh^{III\text{-}LS}$: ${}^1A_{1g} \rightarrow {}^1T_{2g}$ (minor contribution of ${}^1A_{1g} \rightarrow {}^5T_{2g}$)
	C	253	39500	d-d of $Rh^{III\text{-}LS}$: ${}^1A_{1g} \rightarrow {}^1T_{1g}$ (minor contribution of ${}^1A_{1g} \rightarrow {}^3T_{2g}$)
	D	340	29400	d-d of $Rh^{III\text{-}LS}$: ${}^1A_{1g} \rightarrow {}^3T_{1g}$

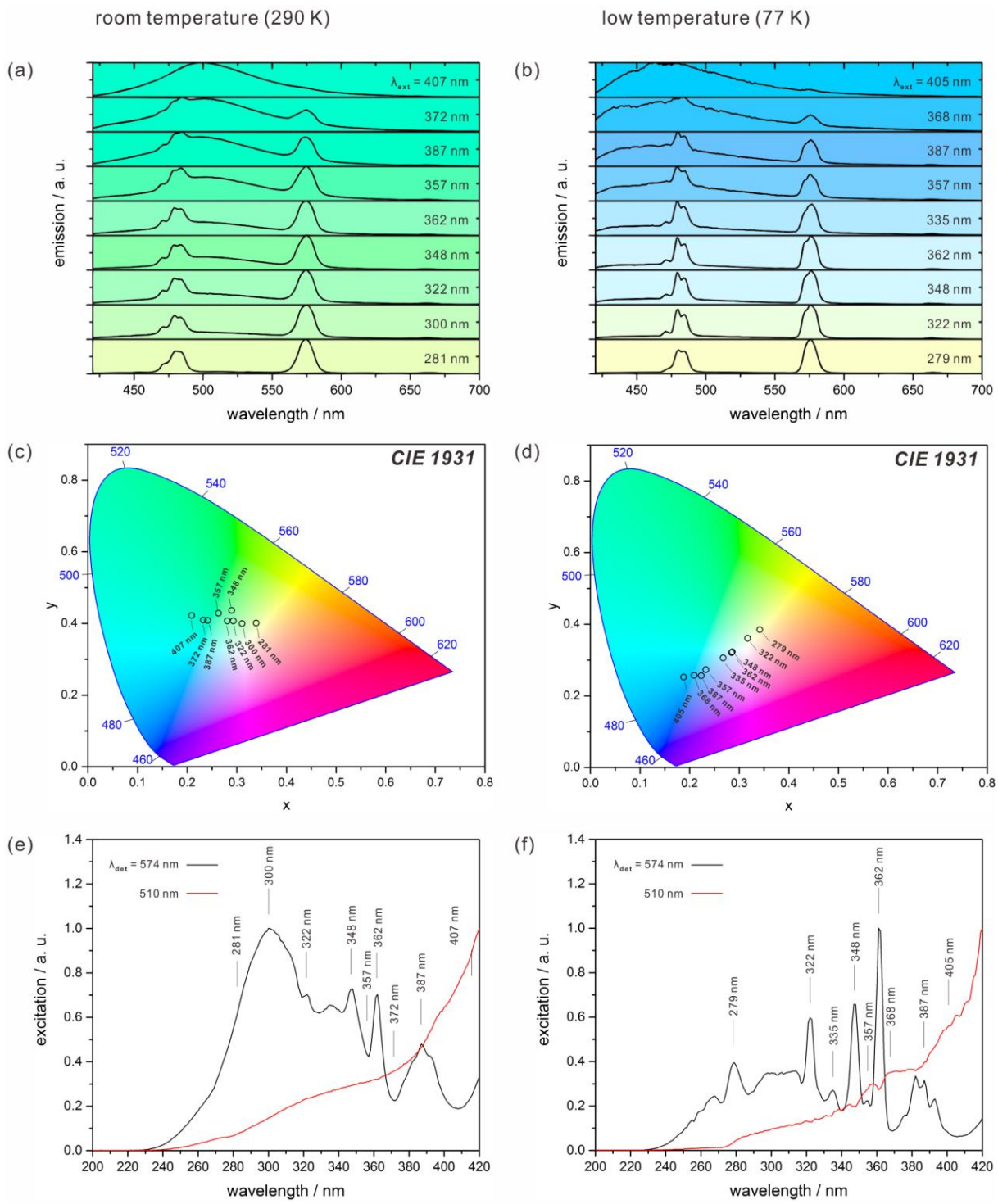

Figure S11 Solid state UV-vis emission spectra of **1** excited by various indicated UV wavelengths (*a*, *b*), together with the resulting emission colours illustrated on the CIE 1931 chromaticity diagrams (*c*, *d*), and the related excitation spectra by the monitoring the pure emission peaks of Dy^{III} (λ_{em} = 574 nm, black line), and 4-pyridone (λ_{em} = 510 nm, red line), respectively (*e*, *f*), at room temperature (290 K, left panel: *a*, *c*, e) and low temperature (77 K, right panel: *b*, *d*, *f*).

Table S7 Summary of *xy* parameters of the CIE 1931 chromaticity scale for the emission colours of **1** under various excitation with indicated wavelengths at room temperature and low temperature (see Figure S10).

T	λ_{exc} / nm	*x*	*y*
room temperature (290 K)	281	0.339	0.401
	300	0.311	0.399
	322	0.293	0.407
	348	0.290	0.436
	362	0.281	0.407
	357	0.263	0.429
	387	0.241	0.408
	372	0.232	0.409
	407	0.209	0.422
low temperature (77 K)	279	0.341	0.385
	322	0.317	0.360
	348	0.286	0.323
	362	0.285	0.321
	335	0.268	0.306
	387	0.224	0.256
	357	0.233	0.273
	368	0.209	0.257
	405	0.188	0.252

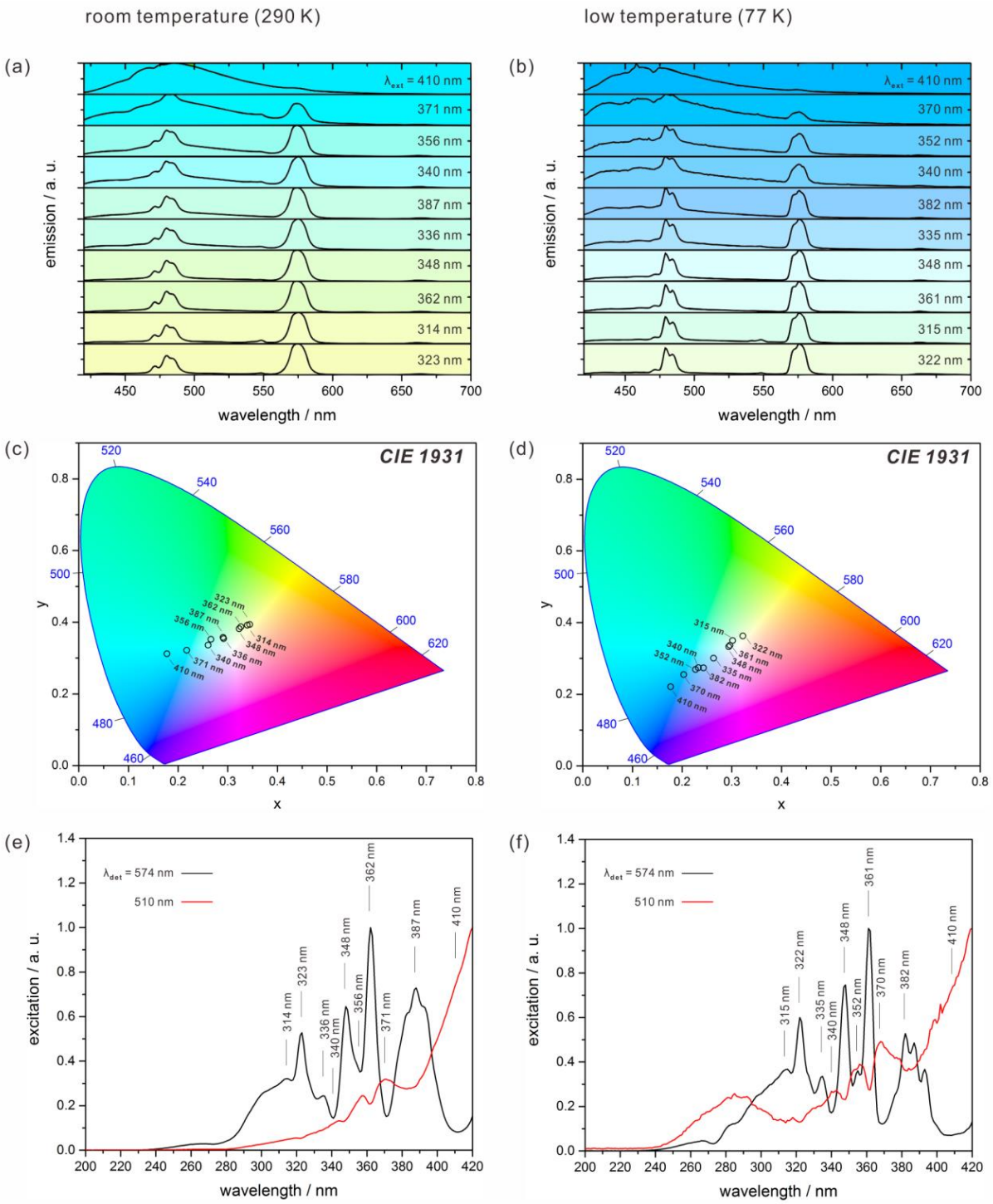

Figure S12 Solid state UV-vis emission spectra of **2** excited by various indicated UV wavelengths (*a*, *b*), together with the resulting emission colours illustrated on the CIE 1931 chromaticity diagrams (*c*, *d*), and the related excitation spectra by the monitoring the pure emission peaks of Dy^{III} (λ_{em} = 574 nm, black line), and 4-pyridone (λ_{em} = 510 nm, red line), respectively (*e*, *f*), at room temperature (290 K, left panel: *a*, *c*, e) and low temperature (77 K, right panel: *b*, *d*, *f*).

Table S8 Summary of *xy* parameters of the CIE 1931 chromaticity scale for the emission colours of **2** under various excitation with indicated wavelengths at room temperature and low temperature (see Figure S11).

T	λ_{exc} / nm	*x*	*y*
room temperature (290 K)	323	0.344	0.393
	314	0.339	0.392
	362	0.327	0.387
	348	0.323	0.382
	336	0.292	0.354
	387	0.291	0.358
	340	0.260	0.336
	356	0.266	0.352
	371	0.217	0.322
	410	0.178	0.312
low temperature (77 K)	322	0.322	0.363
	315	0.302	0.350
	361	0.296	0.337
	348	0.294	0.333
	335	0.263	0.300
	382	0.243	0.274
	340	0.233	0.274
	352	0.227	0.269
	370	0.203	0.255
	410	0.177	0.221

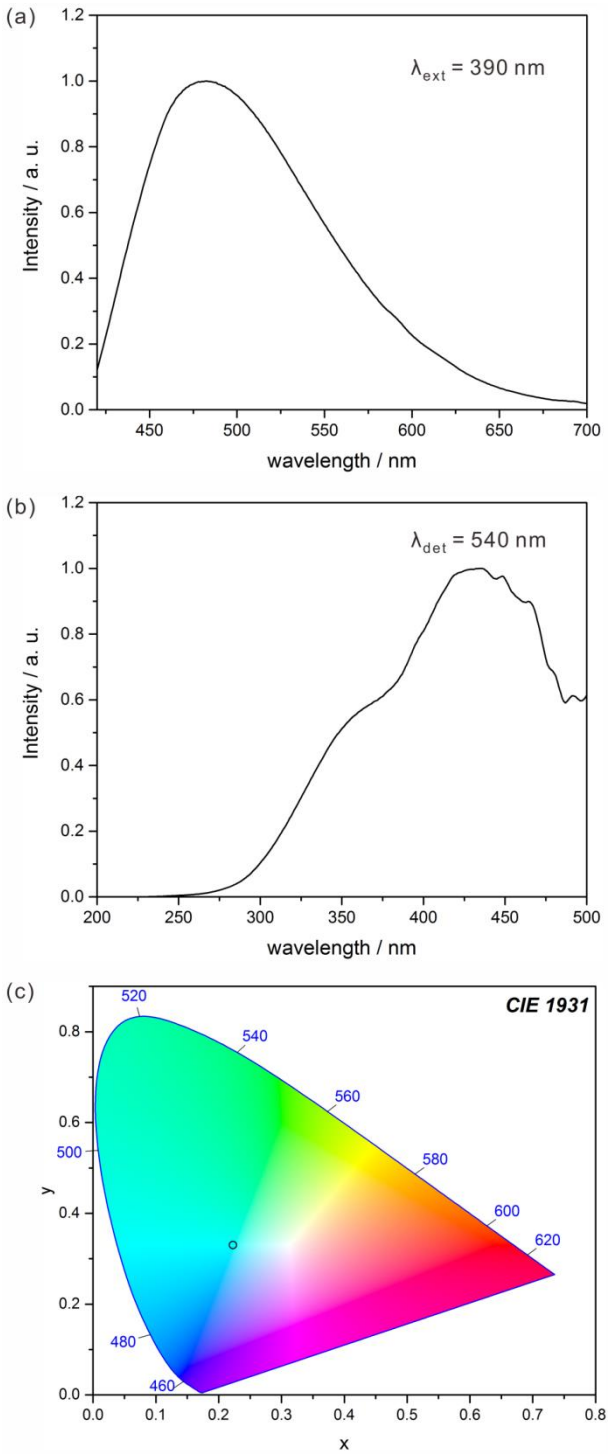

Figure S13 Solid state UV-vis emission spectrum of $K_3[Rh(CN)_6]$ under the excitation light of 390 nm (*a*), the excitation spectrum of $K_3[Rh(CN)_6]$ by the monitored emission at 540 nm (*b*), and the estimated emission colour shown on the CIE 1931 chromaticity diagram (*c*), with *xy* parameters of $x = 0.223$, $y = 0.330$. The measurement was performed at room temperature.

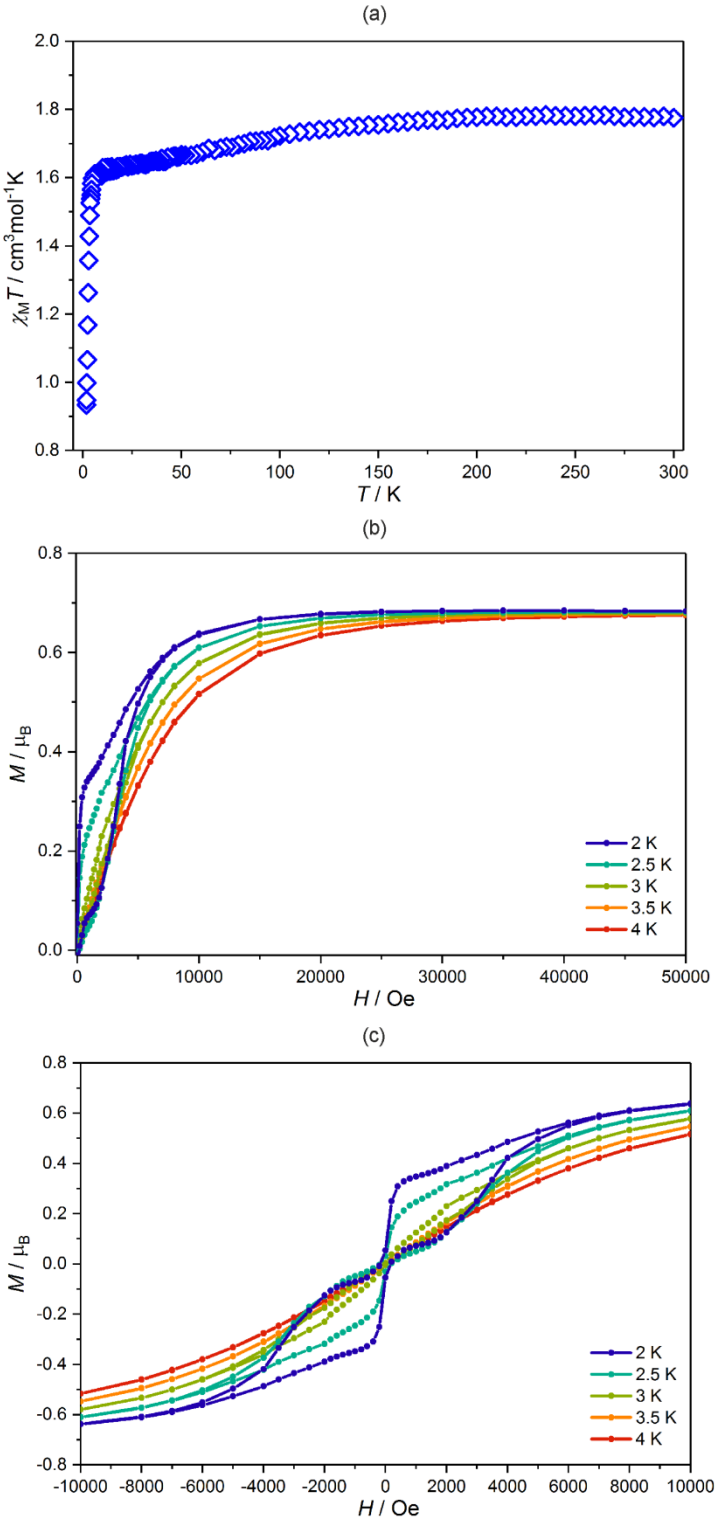

Figure S14 Direct-current (*dc*) magnetic properties of the magnetically diluted sample of **1**, called **1md** (see the comment below): temperature dependence of $\chi_M T$ at H_{dc} = 1000 Oe (*a*), field dependence of molar magnetization, *M*, at indicated temperatures of 2–4 K (*b*), and the butterly-shaped hysteresis loops of the *M*(*H*) plots at indicated temperatures (*c*).

Comment to Figure S14

Synthesis and basic characterization of 1md

In order to investigate deeply the magnetic property of Dy^{III} complexes, the magnetically diluted sample of **1** with diamagnetic yttrium(III), named **1md,** was prepared. Two precursor solutions were prepared as follows. The 0.024 mmol (9 mg) portion of $DyCl_3 \cdot 6H_2O$, the 0.21 mmol (65 mg) portion of YCl_3, and the 2.4 mmol (230 mg) portion of 4-pyridone were dissolved together in the 1.0 ml of distilled water to get solution I, and the 0.24 mmol (80 mg) portion of $K_3[Co(CN)_6]$ was dissolved in the 1.0 ml of distilled water to get solution II. Solution I was heated with stirring, and it was poured into solution II after reaching a boiling point. The resulting solution was filtrated using a vacuum pump after quick stirring for a few seconds, then the vial with the filtrate was left closed for crystallization. After several hours, colourless transparent block-shaped crystals of **1md** were grown in the solution. After one day, the polycrystalline product was collected by a suction filtration, washed by a small portion of water and ethanol, and dried overnight under an air atmosphere, to give 132 mg of the product (yield: 58 %), with the chemical formula of $[(Dy^{III}_{0.12}Y^{III}_{0.88})(4\text{-pyridone})_4(H_2O)_2][Co^{III}(CN)_6] \cdot 2H_2O$ (M_W = 765 g·mol^{-1}). The composition of **1md**, analogous to that found for **1**, was precisely investigated by the CHN elemental analysis of the standard microanalytical method, and thermogravimetric studies. The metal analysis executed by means of inductively couple plasma mass spectrometry (ICP-MS) technique indicated that **1md** contains 12% of Dy^{III}, and 88% of Y^{III}, in terms of the f-metal composition. In addition, the powder X-ray diffraction studies revealed the identical PXRD patterns for both the polycrystalline samples of **1** and **1md**, as well as the pattern simulated from the single-crystal X-ray diffraction model of **1**, which proved that **1** and **1md** are isostructural (Figure S7). Therefore, **1md** can be treated as the magnetically diluted sample of **1**. CHN elemental analysis. Anal. Calcd. for $Dy_{0.12}Y_{0.88}Co_1C_{26}H_{28}N_{10}O_8$ (M_w = 765.3 g·mol^{-1}): C, 40.8 %; H, 3.7 %; N, 18.3 %. Found: C, 40.6 %; H, 3.8 %; N, 18.3 %. TGA: loss of 4 H_2O (two crystallization and two coordinated water molecules), calcd. 9.4 %, found 9.2 % (Figure S2).

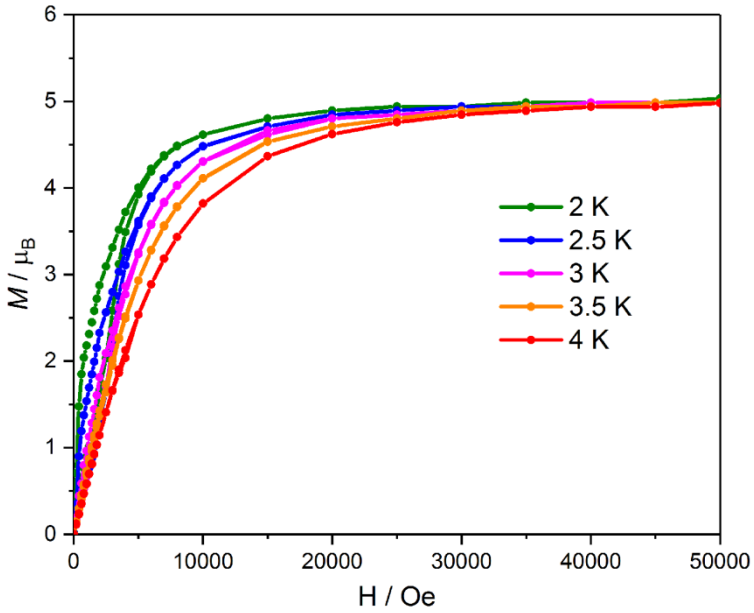

Figure S15 Field dependence of molar magnetization of **1**, *M*, at the indicated temperatures from the 2–4 K range.

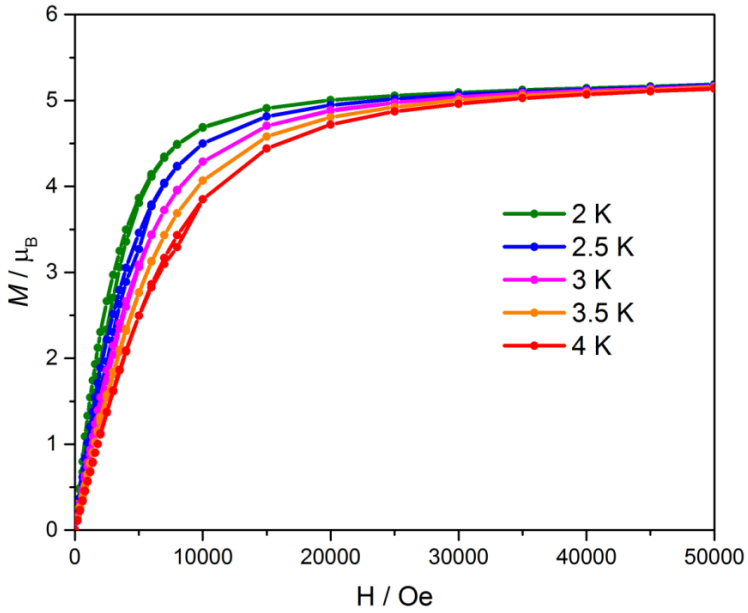

Figure S16 Field dependence of molar magnetization of **2**, *M*, at the indicated temperatures from the 2–4 K range.

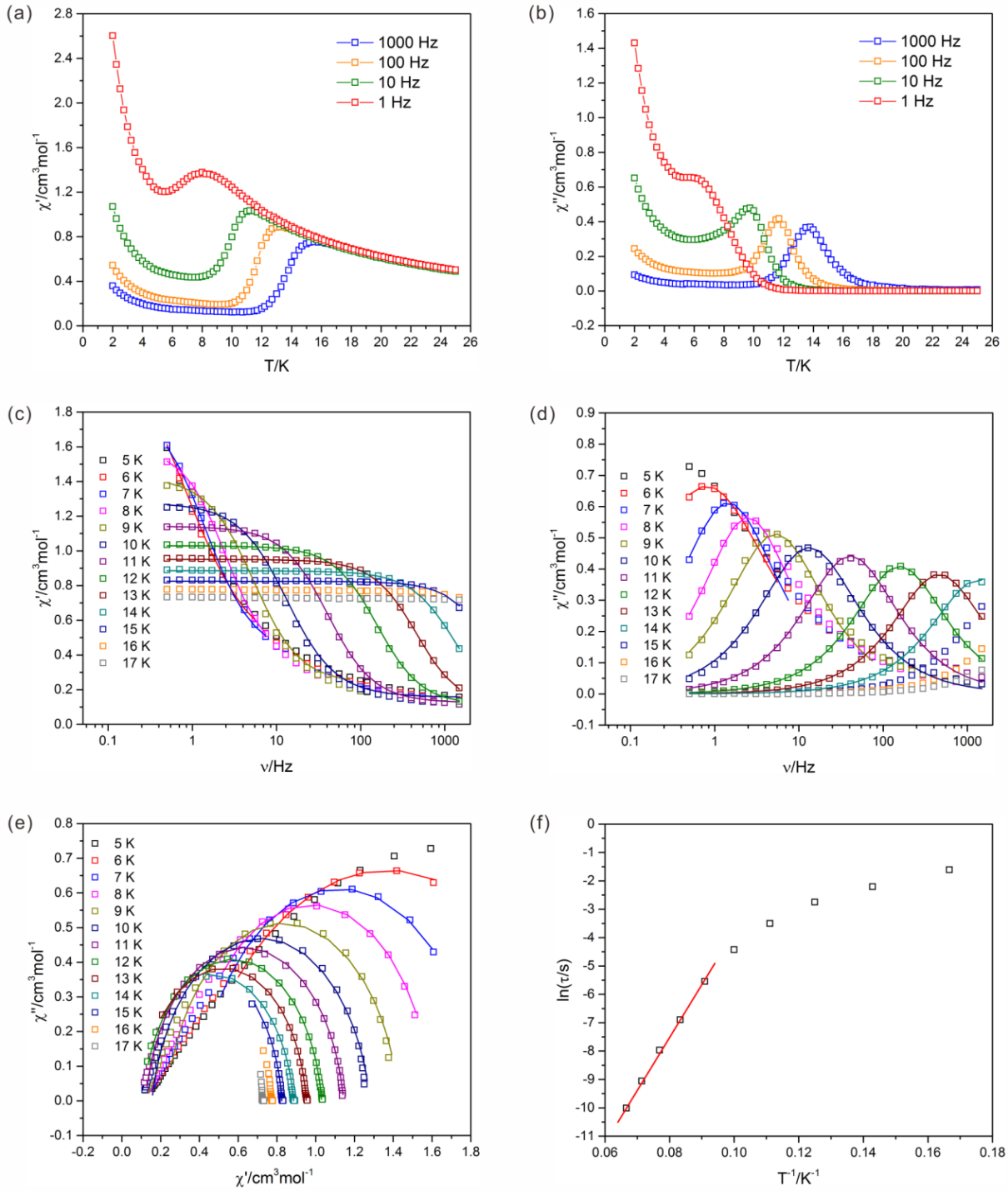

Figure S17 Full *ac* magnetic characteristics of **1** under zero *dc* field with H_{ac} = 3 Oe: temperature dependences of the in-plane, χ_M' (*a*) and out-of-plane, χ_M'' (*b*) components of the complex magnetic susceptibility under indicated frequencies of the 1-1000 Hz range, frequency dependences of the χ_M' (*c*), and χ_M'' (*d*) at indicated temperatures ranging from 5 to 17 K, the related Cole-Cole plots (*e*), the temperature dependence of the relaxation time plotted as ln(τ) versus T^{-1} (*f*). Solid lines in (*c*-*e*) are fitted curves by using the generalized Debye model (Table S9), while the solid line in (*f*) is the fitting following the Arrhenius law ($\ln\tau = \ln\tau_0 - (\Delta E/k_B \cdot T^{-1})$), giving the effective energy barrier, $U_{eff} = \Delta E/k_B$ = 187(6) K, with the pre-exponential factor, $\tau_0 = 1.9(8) \times 10^{-10}$s.

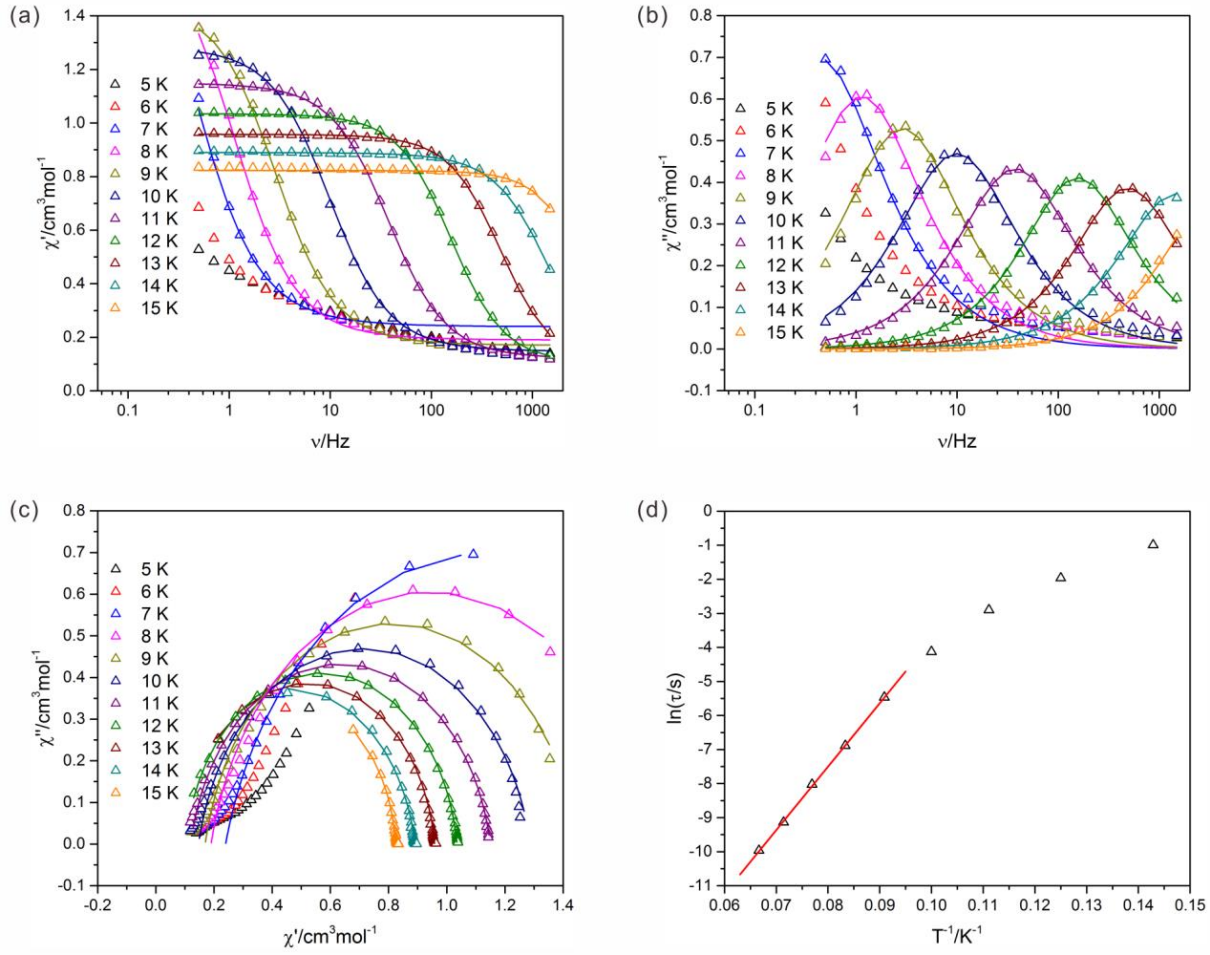

Figure S18 Full *ac* magnetic characteristics of **1** under H_{dc} = 1000 Oe field with H_{ac} = 3 Oe: temperature dependences of the in-plane, χ_M' (*a*) and out-of-plane, χ_M'' (*b*) components of the complex magnetic susceptibility under indicated frequencies of the 1-1000 Hz range, frequency dependences of the χ_M' (*c*), and χ_M'' (*d*) at indicated temperatures ranging from 5 to 17 K, the related Cole-Cole plots (*e*), the temperature dependence of the relaxation time plotted as ln(τ) versus T^{-1} (*f*). Solid lines in (*c*-*e*) are fitted curves by using the generalized Debye model (Table S9), while the solid line in (*f*) is the fitting following the Arrhenius law ($\ln\tau = \ln\tau_0 - (\Delta E/k_B \cdot T^{-1})$), giving the effective energy barrier, $U_{eff} = \Delta E/k_B$ = 186(2) K, with the pre-exponential factor, $\tau_0 = 1.9(3) \times 10^{-10}$s.

Table S9 Fitting parameters of **1** using generalized Debye model for *ac* magnetic data under zero *dc* field (see Figure 16), and under H_{dc} = 1000 Oe (see Figure 17).[S5]

magnetic *dc* field	T / K	χ_S / cm^3mol^{-1}	χ_T / cm^3mol^{-1}	τ / s	α
0 Oe	6	0.350	2.390	0.20	0.264
	7	0.380	1.860	0.110	0.120
	8	0.350	1.60	0.0640	0.0630
	9	0.230	1.430	0.030	0.10
	10	0.155	1.280	0.0120	0.115
	11	0.123	1.143	0.00390	0.090
	12	0.110	0.103	0.00101	0.0750
	13	0.0950	0.951	0.000345	0.070
	14	0.0460	0.886	0.000117	0.0870
	15	0.010	0.830	0.0000450	0.0630
1000 Oe	7	0.240	2.04	0.370	0.160
	8	0.190	1.69	0.140	0.135
	9	0.170	1.45	0.0550	0.120
	10	0.147	1.287	0.0161	0.123
	11	0.120	1.15	0.00422	0.110
	12	0.102	1.035	0.00102	0.080
	13	0.0880	0.958	0.000327	0.075
	14	0.0199	0.890	0.000108	0.096
	15	0.0730	0.823	0.0000470	0.040

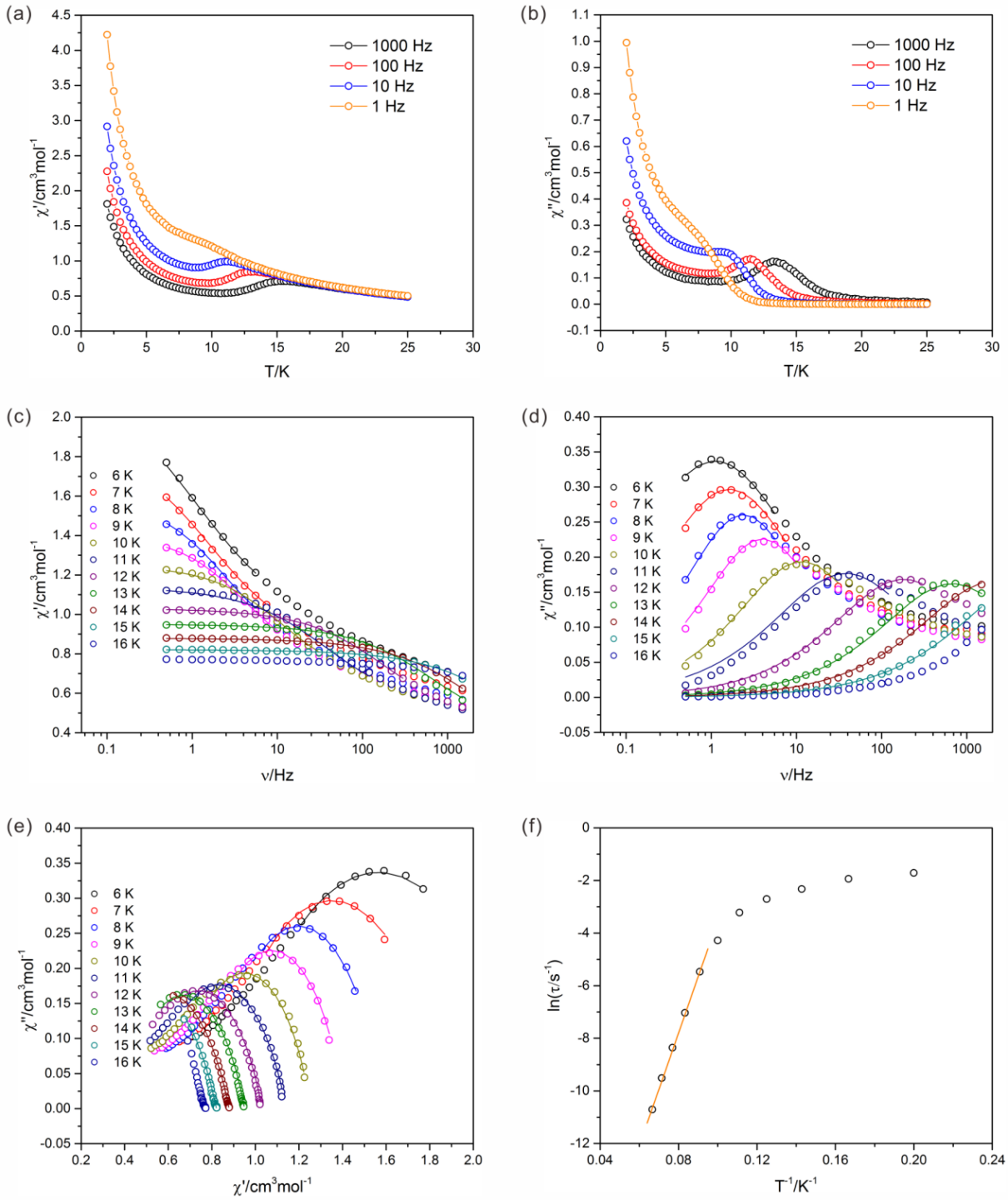

Figure S19 Full *ac* magnetic characteristics of **2** under zero *dc* field with H_{ac} = 3 Oe: temperature dependences of the in-plane, χ_M' (*a*) and out-of-plane, χ_M'' (*b*) components of the complex magnetic susceptibility under indicated frequencies of the 1-1000 Hz range, frequency dependences of the χ_M' (*c*), and χ_M'' (*d*) at indicated temperatures ranging from 5 to 18 K, the related Cole-Cole plots (*e*), the temperature dependence of the relaxation time plotted as ln(τ) versus T^{-1} (*f*). Solid lines in (*c*-*e*) are fitted curves by using the generalized Debye model (Table S10), while the solid line in (*f*) is the fitting following the Arrhenius law ($\ln\tau = \ln\tau_0 - (\Delta E/k_B \cdot T^{-1})$), giving the effective energy barrier, $U_{eff} = \Delta E/k_B$ = 214(4) K, with the pre-exponential factor, $\tau_0 = 1.7(5) \times 10^{-11}$ s.

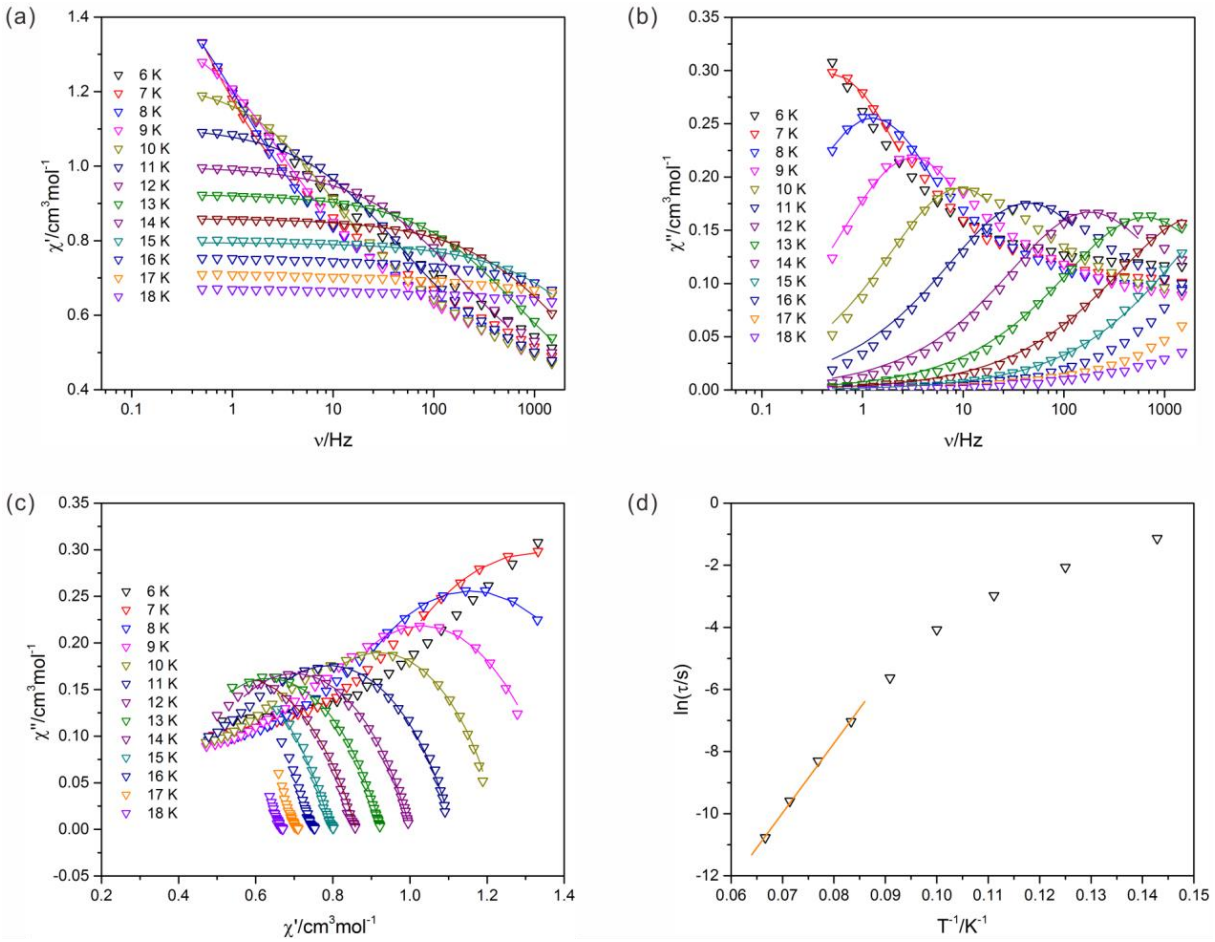

Figure S20 Full *ac* magnetic characteristics of **2** under H_{dc} = 1000 Oe field with H_{ac} = 3 Oe: temperature dependences of the in-plane, χ_M' (*a*) and out-of-plane, χ_M'' (*b*) components of the complex magnetic susceptibility under indicated frequencies of the 1-1000 Hz range, frequency dependences of the χ_M' (*c*), and χ_M'' (*d*) at indicated temperatures ranging from 5 to 18 K, the related Cole-Cole plots (*e*), the temperature dependence of the relaxation time plotted as ln(τ) versus T^{-1} (*f*). Solid lines in (*c*-*e*) are fitted curves by using the generalized Debye model (Table S10), while the solid line in (*f*) is the fitting following the Arrhenius law ($\ln\tau = \ln\tau_0 - (\Delta E/k_B \cdot T^{-1})$), giving the effective energy barrier, $U_{eff} = \Delta E/k_B$ = 224(8) K, with the pre-exponential factor, $\tau_0 = 7(5) \times 10^{-12}$s.

Table S10 Fitting parameters of **2** using generalized Debye model for *ac* magnetic data under zero *dc* field (see Figure 18), and under H_{dc} = 1000 Oe (see Figure 19).[S5]

magnetic *dc* field	T / K	χ_S / cm^3mol^{-1}	χ_T / cm^3mol^{-1}	τ / s	α
0 Oe	6	0.87	2.26	0.144	0.425
	7	0.81	1.89	0.098	0.36
	8	0.81	1.59	0.067	0.25
	9	0.741	1.406	0.04	0.24
	10	0.643	1.253	0.0138	0.28
	11	0.52	1.14	0.0042	0.34
	12	0.45	1.03	0.00088	0.33
	13	0.39	0.95	0.000235	0.332
	14	0.279	0.879	0.000074	0.355
	15	0.181	0.821	0.0000224	0.37
1000 Oe	7	0.78	1.88	0.32	0.37
	8	0.705	1.61	0.127	0.345
	9	0.67	1.39	0.051	0.305
	10	0.61	1.23	0.017	0.3
	11	0.47	1.11	0.0036	0.36
	12	0.4	1	0.000881	0.352
	13	0.34	0.925	0.000248	0.355
	14	0.24	0.86	0.000068	0.379
	15	0.14	0.795	0.000021	0.365

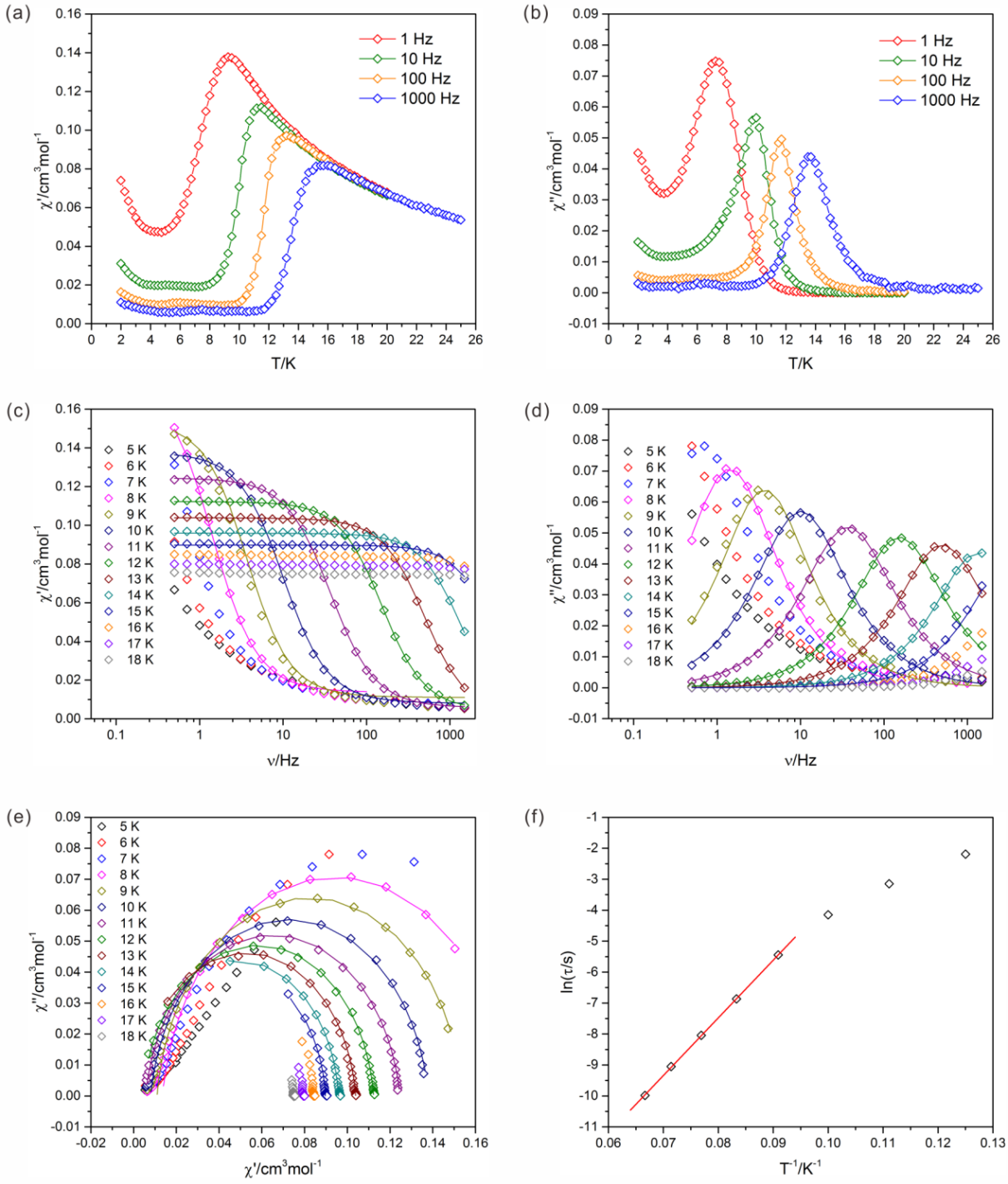

Figure S21 Full *ac* magnetic characteristics of **1md** under zero *dc* field with H_{ac} = 3 Oe: temperature dependences of the in-plane, χ_M' (*a*) and out-of-plane, χ_M'' (*b*) components of the complex magnetic susceptibility under indicated frequencies of the 1-1000 Hz range, frequency dependences of the χ_M' (*c*), and χ_M'' (*d*) at indicated temperatures ranging from 5 to 18 K, the related Cole-Cole plots (*e*), the temperature dependence of the relaxation time plotted as ln(τ) versus T^{-1} (*f*). Solid lines in (*c*-*e*) are fitted curves by using the generalized Debye model (Table S10), while the solid line in (*f*) is the fitting following the Arrhenius law ($\ln\tau = \ln\tau_0 - (\Delta E/k_B \cdot T^{-1})$), giving the effective energy barrier, $U_{eff} = \Delta E/k_B$ = 186(1) K, with the pre-exponential factor, $\tau_0 = 1.89(17) \times 10^{-10}$ s.

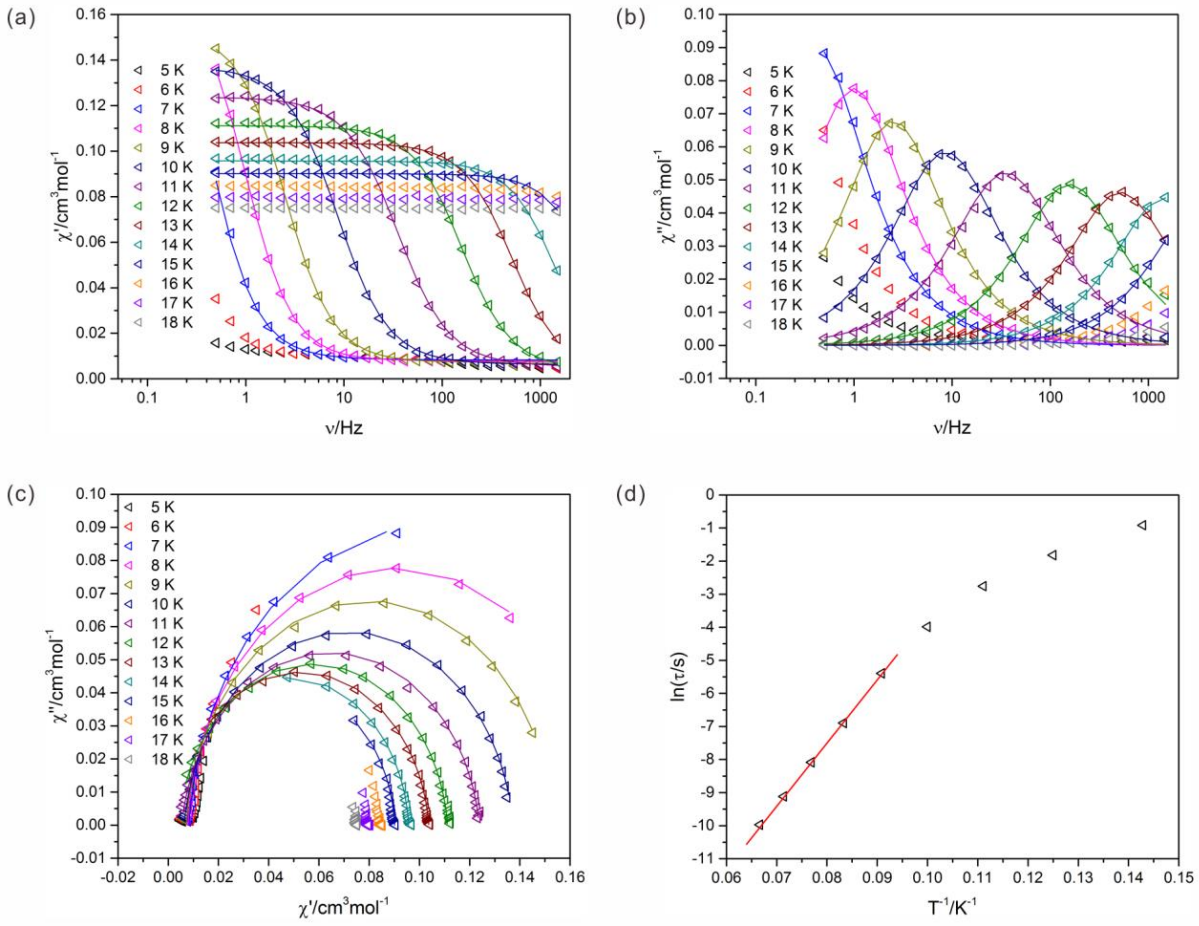

Figure S22 Full *ac* magnetic characteristics of **1md** under H_{dc} = 1000 Oe with H_{ac} = 3 Oe: temperature dependences of the in-plane, χ_M' (*a*) and out-of-plane, χ_M'' (*b*) components of the complex magnetic susceptibility under indicated frequencies of the 1-1000 Hz range, frequency dependences of the χ_M' (*c*), and χ_M'' (*d*) at indicated temperatures ranging from 5 to 18 K, the related Cole-Cole plots (*e*), the temperature dependence of the relaxation time plotted as ln(τ) versus T^{-1} (*f*). Solid lines in (*c*-*e*) are fitted curves by using the generalized Debye model (Table S10), while the solid line in (*f*) is the fitting following the Arrhenius law ($\ln\tau = \ln\tau_0 - (\Delta E/k_B \cdot T^{-1})$), giving the effective energy barrier, $U_{eff} = \Delta E/k_B$ = 191(2) K, with the pre-exponential factor, $\tau_0 = 1.25(14) \times 10^{-10}$ s.

Table S10 Fitting parameters of **1md** using generalized Debye model for *ac* magnetic data under zero *dc* field (see Figure 20), and under H_{dc} = 1000 Oe (see Figure 21).[S5]

magnetic *dc* field	T / K	χ_S / cm^3mol^{-1}	χ_T / cm^3mol^{-1}	τ / s	α
0 Oe	8	0.0135	0.1755	0.112	0.086
	9	0.011	0.154	0.043	0.07
	10	0.008	0.138	0.01582	0.0833
	11	0.0056	0.1246	0.00431	0.085
	12	0.0043	0.1123	0.00104	0.066
	13	0.0015	0.1039	0.0003205	0.065
	14	0.0009	0.0959	0.000117	0.051
	15	0.0008	0.0898	0.000046	0.046
1000 Oe	7	0.0083	0.2043	0.4	0.05
	8	0.0078	0.1738	0.162	0.042
	9	0.0072	0.1532	0.0633	0.047
	10	0.0063	0.1373	0.01853	0.072
	11	0.00535	0.12385	0.00454	0.08
	12	0.0042	0.1112	0.00101	0.06
	13	0.00175	0.10375	0.000308	0.062
	14	0.0002	0.0957	0.00011	0.043
	15	0.0015	0.0901	0.0000466	0.035

References to Supporting Information

[S1] (a) M. Llunell, D. Casanova, J. Cirera, J. Bofill, P. Alemany, S. Alvarez, M. Pinsky and D. Avnir, *SHAPE v. 2.1. Program for the Calculation of Continuous Shape Measures of Polygonal and Polyhedral Molecular Fragments*, University of Barcelona: Barcelona, Spain, 2013; (b) D. Casanova, J. Cirera, M. Llunell, P. Alemany, D. Avnir and S. Alvarez, *J. Am. Chem. Soc*. 2004, **126**, 1755.

[S2] (a) J. Feng, H.-J. Zhang, S.-Y. Song, Z.-F. Li, L.-N. Sun, Y. Xing and X.-M. Guo, *J. Lumin.* 2008, **128**, 1957; (b) J. Feng, L. Zhou, S.-Y. Song, Z.-F. Li, W.-Q. Fan, L.-N. Sun, Y.-N. Yu and H.-J. Zhang, *Dalton Trans.* 2009, 6593; (c) G. Kaur and S. B. Rai, *J. Fluoresc.* 2012, **22**, 475; (d) E. Pavitra, G. Seeta Rama Raju, W. Park and J. Su Yu, *New J. Chem.* 2014, **38**, 163; (e) D. D. Ramteke and R. S. Gedam, *Spectr. Lett.* 2015, **48**, 417.

[S3] (a) A. Weisstuch, P. Neidig and A. C. Testa, *J. Lumin.* 1975, **10**, 137; (b) P. Beak, F. S. Fry, J. Lee and F. Steele, *J. Am. Chem. Soc*. 1976, **98**, 171; (c) S. Hotchandani and A. C. Testa, *J. Chem. Phys*. 1977, **67**, 5201.

[S4] (a) V. M. Miskowski, H. B. Gray, R. B. Wilson and E. I. Solomon, *Inorg. Chem.* 1979, **18**, 1410; (b) H. Kunkely and A. Vogler, *Inorg. Chem. Commun.* 2004, **7**, 770; (c) T. Lazarides, G. M. Davies, H. Adams, C. Sabatini, F. Barigelletti, A. Barbieri, S. J. A. Pope, S. Faulkner and M. D. Ward, *Photochem. Photobiol. Sci.* 2007, **6**, 1152; (d) J. J. Alexander, H. B. Gray, *Coord. Chem. Rev.* 1967, **2**, 29.

[S5] (a) Y.-N. Guo, G.-F. Xu, Y. Guo and J. Tang, *Dalton Trans*. 2011, **40**, 9953; (b) M. Ramos Silva, P. Martin- Ramos, J. T. Coutinho, L. C. J. Pereira and J. Martin-Gil, *Dalton Tran*s. 2014, **43**, 6752; (c) S. Chorazy, J. Wang and S. Ohkoshi, *Chem. Commun*. 2016, **52**, 10795.